Interdisciplinary Fracture Network Characterization in the Crystalline Basement: A case study from the Southern Odenwald, SW Germany

Matthis Frey[1], Claire Bossennec[1], Lukas Seib[1], Kristian Bär[1], Eva Schill[1,2], Ingo Sass[1,3]

[1]Technical University of Darmstadt, Institute of Applied Geosciences, Department of Geothermal Science and Technology, Schnittspahnstraße 9, 64287 Darmstadt, Germany

[2]Karlsruher Institut für Technologie, Hermann-von-Helmholtz Platz 1

[3]GFZ German Research Centre for Geosciences, Section 4.8: Geoenergy, Telegrafenberg, 14473 Potsdam, Germany

Correspondence to: Matthis Frey (frey@geo.tu-darmstadt.de, ORCID: 0000-0003-2284-4215)

Abstract. The crystalline basement is considered a ubiquitous and almost inexhaustible source of geothermal energy in the Upper Rhine Graben and other regions worldwide. The hydraulic properties of the basement, which are one of the key factors for the productivity of geothermal power plants, are primarily controlled by hydraulically active faults and fractures. While the most accurate in situ information about the general fracture network is obtained from image logs of deep boreholes, such data are generally sparse, costly and thus often not openly accessible. To circumvent this problem, an outcrop analogue study with interdisciplinary geoscientific methods was conducted in the Tromm Granite, located in the southern Odenwald at the northeastern margin of the URG. Using Light detection and ranging (LiDAR) scanning, the key characteristics of the fracture network were extracted in a total of five outcrops, additionally complemented by lineament analysis of two different digital elevation models (DEMs). Based on this, discrete fracture network (DFN) models were developed to calculate equivalent permeability tensors under assumed reservoir conditions. The influence of different parameters, such as fracture orientation, density, aperture and mineralization was investigated. In addition, extensive gravity and radon measurements were carried out in the study area, allowing to map fault zones with naturally increased porosity and permeability. Gravity anomalies served as input data for a stochastic density inversion, through which areas of potentially increased open porosity were identified. A laterally heterogeneous fracture network characterizes the Tromm Granite, with the highest natural permeabilities expected at the pluton margin, due to the influence of large shear and fault zones.

1 Introduction

The Upper Rhine Graben (URG) represents a region with a high potential for deep geothermal projects in Central Europe due to a significantly increased geothermal gradient of locally more than 100 °C km^{-1} (e.g. Agemar et al., 2014). Often based on knowledge from hydrocarbon production, exploration of geothermally relevant depths began in the 1980s, allowing to build on decades of experience (Dezayes et al., 2005a; Cuenot et al., 2008; Genter et al., 2010). Convective heat transport along active large-scale fault zones has been identified as the main reason for the elevated temperatures at shallow depth (Bächler et al., 2003; Baillieux et al., 2013; Guillou-Frottier et al., 2013; Duwiquet et al., 2021). Besides, the resulting thermal anomalies are supported by the graben-wide radiogenic heat production, increased heat flux from the mantle and thermal blanketing effect resulting from the low thermal conductivity of the thick sedimentary cover (Freymark et al., 2017). When exploiting the resulting vast potential, reservoirs with sufficient natural permeability are aimed at to ensure economically viable fluid production. In this context, the top of the crystalline basement in the URG presents an attractive target. In this part of the basement, the abundance of fractures and faults often enables substantial natural fluid flow (Sausse and Genter, 2005; Vidal et al., 2017; Dezayes et al., 2021; Glaas et al., 2021). Examples of successful geothermal production from the crystalline basement in the URG are the EGS (enhanced geothermal system) projects in Insheim, Landau, Rittershoffen and Soultz-sous-Forêts (Schill et al., 2017; Vidal and Genter, 2018).

Fluid flow in fractured reservoirs depends on a multitude of parameters and processes, such as the density, orientation, length, opening and roughness of fractures, stress conditions or the influence of mineralization (Stober and Bucher, 2007; Ledésert et al., 2010; Bisdom et al., 2017; Meller and Ledésert, 2017). Consequently, it is essential to characterize and quantify the properties of the fracture network. The most reliable discrete fracture network (DFN) models have been obtained from geophysical logs in combination with vertical seismic profiling (Genter and Traineau, 1996; Genter et al., 1997; Dezayes et al., 2010; Sausse et al., 2010; Schill et al., 2017; Afshari et al., 2019; Glaas et al., 2021). However, drillings in the crystalline basement of the URG are generally sparse. Furthermore, models of fracture networks from wells and VSP lack in information on the fracture length, the aperture and the fracture mineralization in particular for small-sized fractures. Thus, with increasing distance to deep boreholes, also the uncertainty related to the organization and properties of the fracture network increases.

New insights and especially a better spatial and multi-scale understanding of the fracture network characteristics can be gained by investigating the exposed crystalline rocks at the graben shoulders as an outcrop analogue for the URG basement (Weinert et al., 2020; Dezayes et al., 2021). The presented greenfield case study focuses on the Tromm Granite in the southern Odenwald (Fig. 1). This highly fractured granitic pluton is relatively homogenous with respect to lithology and is representative for the predominantly granitoid basement in the northern URG (Frey et al., 2021a). Furthermore, the Tromm Granite is a promising site for the geothermal underground research laboratory GeoLaB (Schill et al., 2016), where thermal-hydraulic-mechanical-chemical processes on fractures will be investigated in the future to minimize the risk of future enhanced geothermal systems. The characterization of fracture networks in the Tromm Granite was performed using a combination of established techniques on multipe scales. Outcrops distributed over the entire pluton were analyzed using the Light Image Detection And Ranging

(LiDAR) technique (Fisher et al., 2014; Biber et al., 2018; Zeng et al., 2018). Visible fractures were identified and the relevant structural parameters were extracted. This dataset is supplemented by the examination of lineaments in two digital elevation models (DEMs) with 1 m and 1 arcsecond resolution, following the approaches of Pickering et al. (1995), Guerriero et al. (2011), Bertrand et al. (2015) and Meixner et al. (2018). Based on this dataset, DFN models were developed, from which the effect of various fracture network parameters on the hydraulic properties of the crystalline basement can be inferred. Because major faults are not outcropping in the area, fault zones were characterized by surface gravity measurements as shown by Guglielmetti et al. (2013), Altwegg et al. (2015) and Deckert et al. (2017). The stochastic inversion of these gravity data allows estimating the porosity in the granite (e.g. Li and Oldenburg, 1998). Moreover, permeable fault zones were indicated by radon measurements (Ioannides et al., 2003; King et al., 1996; Jolie et al., 2015). As a result, a comprehensive multidisciplinary data set was obtained that is unique for a crystalline outcrop analogue. The integrated approach provides insights into the permeability structure of the basement, which are partially transferable to reservoirs of comparable lithology and structural configuration in the URG.

2 Geological framework

The crystalline Odenwald at the northeastern margin of the URG is the largest outcrop of the Mid-German Crystalline High (MGCH), extending over 50 km from Heidelberg to Darmstadt (Fig. 1). This complex is usually subdivided into the two petrogenetic units Bergsträßer and Böllsteiner Odenwald, which are separated by a large-scale sinistral shear zone, called Otzberg Shear Zone (Amstutz et al., 1975; Stein, 2001; Schälicke, 1975). The older Böllsteiner Odenwald, located in the east, consists mainly of dome-shaped granitoid orthogneisses whose protoliths were emplaced during the Lower Devonian (Altenberger and Besch, 1993; Reischmann et al., 2001).

In comparison, the Bergsträßer Odenwald is dominated by Variscan plutonic rocks intruded into a metamorphic volcanic-sedimentary series (Altherr et al., 1999). The relics of these host rocks, commonly referred to as Schieferzüge (shale and gneiss bands), comprise gneisses, mica schists, amphibolites and scarcely marble (Okrusch et al., 1975). From north to south, the exposed basement rocks show a gradual transition from a primitive island arc regime to a collisional setting (Okrusch et al., 1995; Altherr et al., 1999). While the relatively older northern Frankenstein Complex (intrusion ages 362 ± 7 Ma; Todt et al., 1995) exhibits a primarily mafic composition, the southern plutons are predominantly felsic. For the latter, hornblende and biotite ages between 326 and 336 Ma and an intrusion depth of 15 to 19 km were determined (Kreuzer and Harre, 1975). The emplacement of granitoids in the Carboniferous occurred during a syn-orogenic phase in an overall transtensional to extensional setting, as evidenced by large-scale strike-slip and normal faults, separating the individual magmatic and metamorphic units (Krohe, 1991; Krohe and Willner, 1995). These conditions are likely related to oblique subduction of the Rheic or Rhenohercynian basins and associated back-arc spreading. Mineral alignment within the plutonic rocks indicates plastic deformation during crystallization (Krohe, 1992). With progressive cooling, the increasingly brittle deformation was concentrated in large fault zones (Hess and Schmidt, 1989).
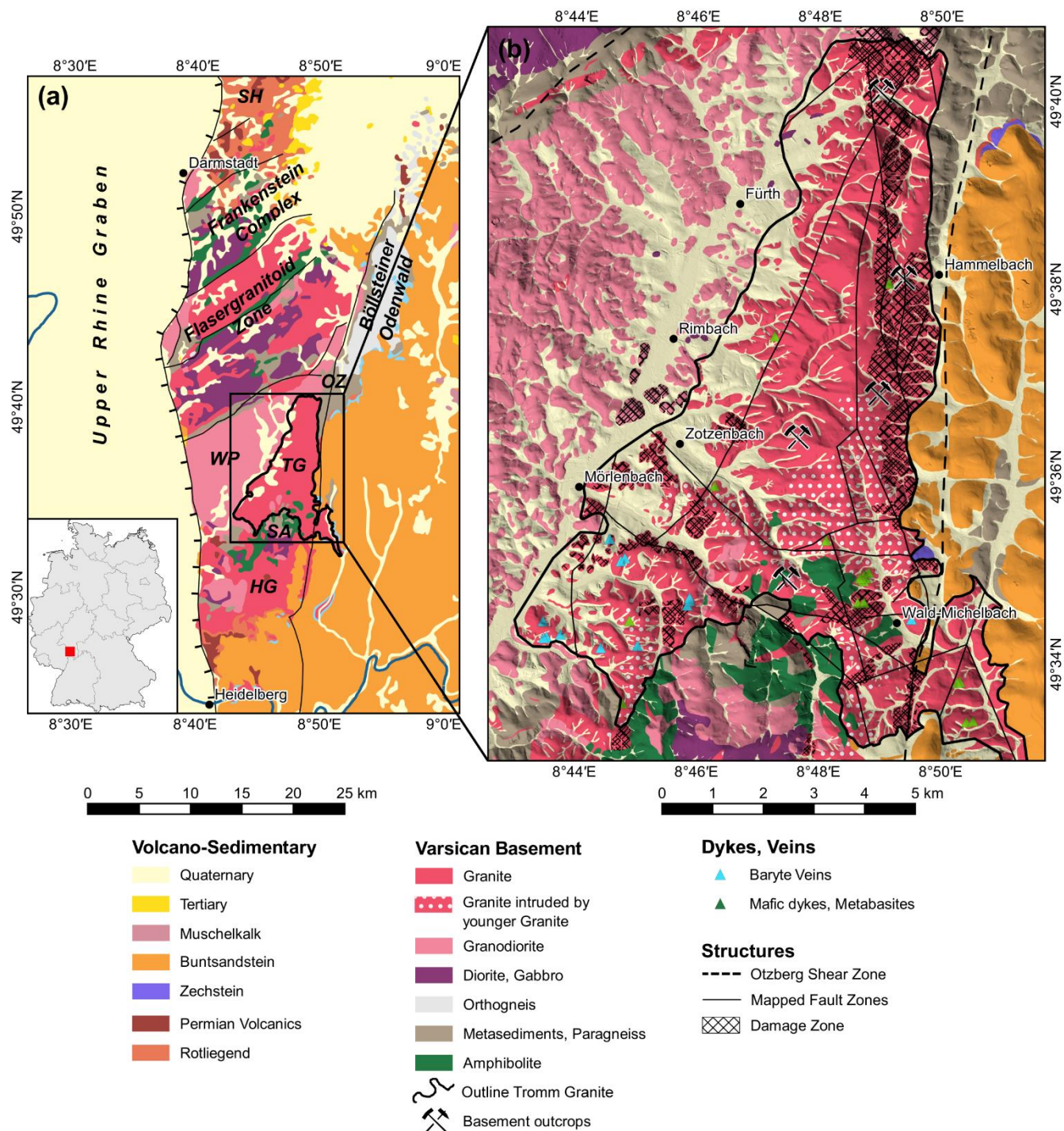
Figure 1: Overview of the study area: (a) geological map of the Odenwald (modified after HLUG, 2007); (a) geological map of the Tromm Granite in the southern Odenwald (Klemm, 1900, 1928, 1929, 1933). Mapped fault zones have been compiled from various

The Tromm Granite forms an c. 60 km² large wedge between the Weschnitz Pluton to the west and the metamorphic Böllsteiner Odenwald to the east. The Tromm Granite is a medium to coarse-grained, orthoclase-rich, biotite-bearing and often reddish granite, containing large potassium feldspar inclusions (Maggetti, 1975). Locally, the rock gradually merges into granodiorite and mixed specimens can be observed. The southern part between Zotzenbach and Wald-Michelbach exhibits a fine-grained variety of the Tromm Granite of similar mineralogical composition and of younger age than the coarser variety. In several locations, the granite is intruded by different generations of granitic, aplitic or pegmatitic dykes and veins (Klemm, 1933).
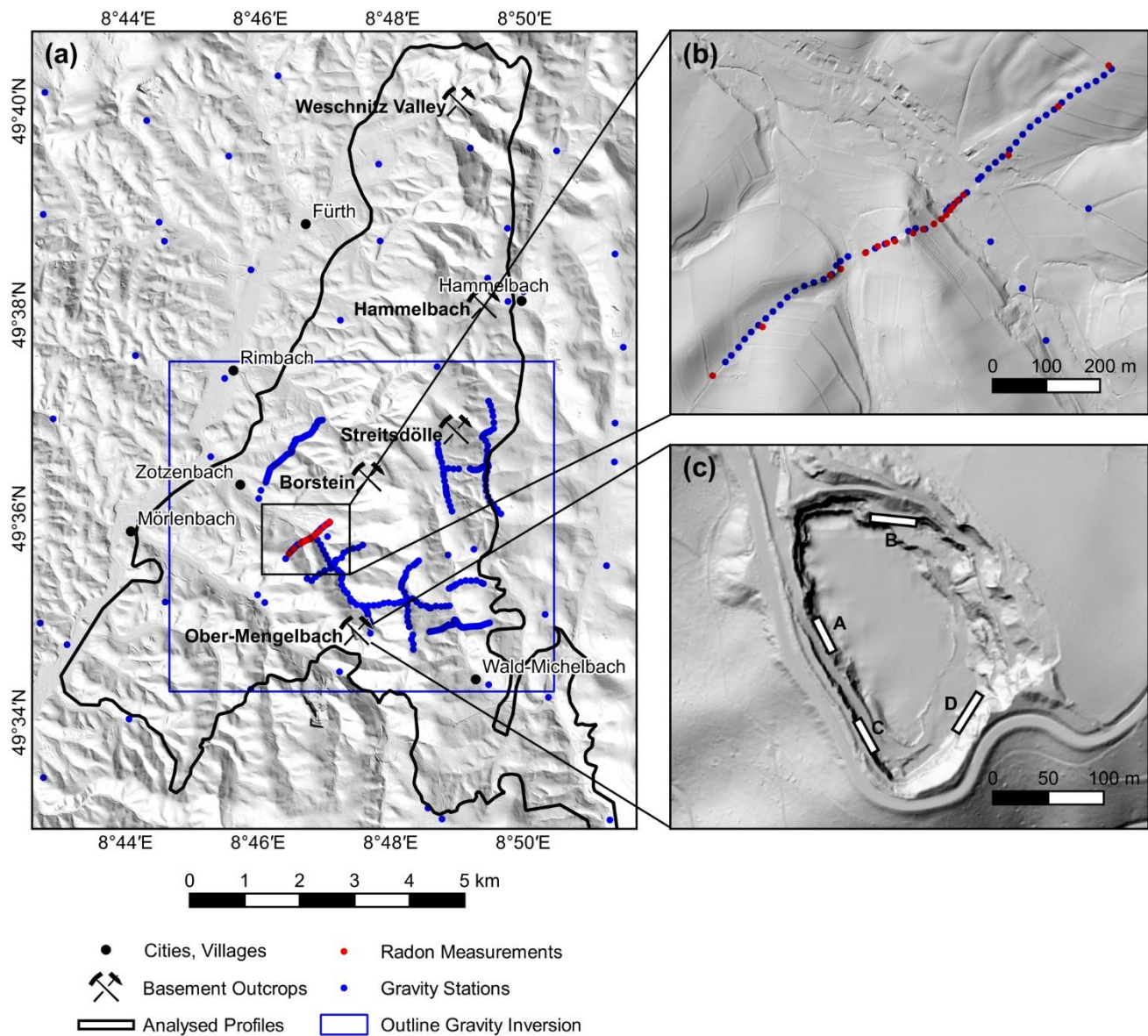
While an interlocking of the two plutons characterizes the contact between the Tromm Granite with the Weschnitz Granodiorite, the eastern boundary constitutes a 1-2 km wide heterogeneous westward dipping mylonitization and cataclasic zone along the Otzberg Fault (Schälicke, 1975; Hess and Schmidt, 1989). In the southeast, parts of this zone are overlain by Buntsandstein. To the south, the pluton is bounded by the so-called Schollenagglomerat (Nickel, 1975). This is presumably a former Schieferzug, which was dismantled into separate blocks by shear movements along the Otzberg Shear Zone and by the intrusion of the Tromm Granite (Schälicke, 1975). The remaining amphibolite-facies overprinted rocks are often strongly intruded and assimilated by granitic dykes. The amphibolites are derived from mafic volcanic rocks or tuffs, whereas the gneisses and mica schists are rather of paragenic origin (Todt et al., 1995; Poller et al., 2001; Schubert et al., 2001).

Most of the mapped and interpreted faults strike NNE-SSW to NNW-SS, which approximately corresponds to the orientation of s_{Hmax} (130° to 165°) measured in the northern URG (Reiter et al., 2016). A secondary direction is present in the WNW-ESE. Lamprophyric dykes in the mylonites of the Otzberg Shear Zone, are dated at 330 Ma, suggesting that most of the shearing along this zone occurred shortly after the emplacement of the Tromm Granite (Hess and Schmidt, 1989). Later reactivations during Permian rifting or the opening of the URG in the Cenozoic are likely, as indicated by the vertical offset of post-Variscan sediments at the eastern margin of the Tromm Granite, locally reaching several hundred meters (Klemm, 1933). It is generally difficult to assess the age of the faults where no sediments are preserved for correlation and mineralizations within the faults are not dated.

3 Material and Methods

The interdisciplinary and multi-scale fracture network characterization is carried out using the following methods. The first part focuses on structural geological investigations and DFN modelling. The second part presents the applied geophysical acquisition techniques in detail. A summary of all investigations in the Tromm Granite is given in Fig. 2.

5

Figure 2: Overview map of the surveys conducted in the Tromm Granite: (a) locations of structural and geophysical data acquisitions; (b) detailed view of the combined gravity and radon profile; (c) detailed view of the quarry in Ober-Mengelbach with the location of 2D profiles, which have been manually interpreted. Digital elevation model provided by the HVBG (Hessische Verwaltung für Bodenmanagement und Geoinformation).

3.1 Structural investigations

3.1.1 Lineament analysis

130

Two DEMs of the Tromm Granite were examined with respect to the density, length and orientation of lineaments. The high-resolution DEM with a cell size of 1 m allowed detailed structural investigations. In addition, the satellite-based SRTM model with a resolution of 1 arcsecond was used to identify regional structural features.

Lineaments are natural, rectilinear surface features that are uniquely identifiable and likely reflect subsurface structures, i.e.,

135 faults, discontinuities, or weakness zones. It should be noted that shallow dipping faults may not appear as linear structures and thus may be underrepresented, especially in areas of strong relief. However, most faults in the Tromm Granite are assumed to be rather steeply dipping.

The methodology of lineament analysis is described in previous studies, e.g. in Bertrand et al. (2015), Meixner et al. (2018) or Bossennec et al. (2021). The software QGis was used to generate hill shade maps of the DEMs, which were then visually

140 inspected for lineaments. To avoid misinterpretation, four different illumination azimuths of the hill shades maps (90°, 135°, 180°, and 225°) were compared and the results were checked for anthropogenic structures such as roads or other buildings. The digitized lineaments were used to calculate the lineament density P20 (number of fractures per unit area) and intensity P21 (total length of fractures per unit area) (Sanderson and Nixon, 2018).

3.1.2 Outcrop analysis

145 Five abandoned quarries located across the Tromm Granite were selected for detailed structural analysis of the fracture network (Fig. 2). As also described in Bossennec et al. (2021), the RIEGL VG 400 LiDAR instrument was used to generate high-resolution point clouds (point spacing ≤ 1 cm) of the outcrop walls. Compared to classical scanlines, this approach allows for relatively quick acquisition of large structural datasets. At the same time, the statistical bias is reduced as all visible fractures are detected, not only those that cross a 1D line. For an in-depth discussion of the reliability of LiDAR for outcrop analysis,

150 see Biber et al. (2018), Fisher et al. (2014), Vazaios et al. (2017) or Zeng et al. (2018).

The raw LiDAR data were first imported into RiSCAN PRO to merge individual scans. Further analysis of the point clouds was performed using the open-source softwares CloudCompare and QGis. The point cloud was resampled to less than 2 million points to reduce the computational effort of the following steps. Afterwards, the orientation of the surface normals was calculated by triangulation between the points and converted to dip and dip direction. Based on this, the Ransac shape detection

155 plugin was applied to automatically extract the orientation of continuous fracture planes (e.g. Drews et al., 2018). The following parameters were chosen for this step: maximum distance to plane = 5 cm, scanning distance = 20 cm, maximum normal deviation = 10°. Each detected plane was visually inspected and removed if it did not represent natural fractures.
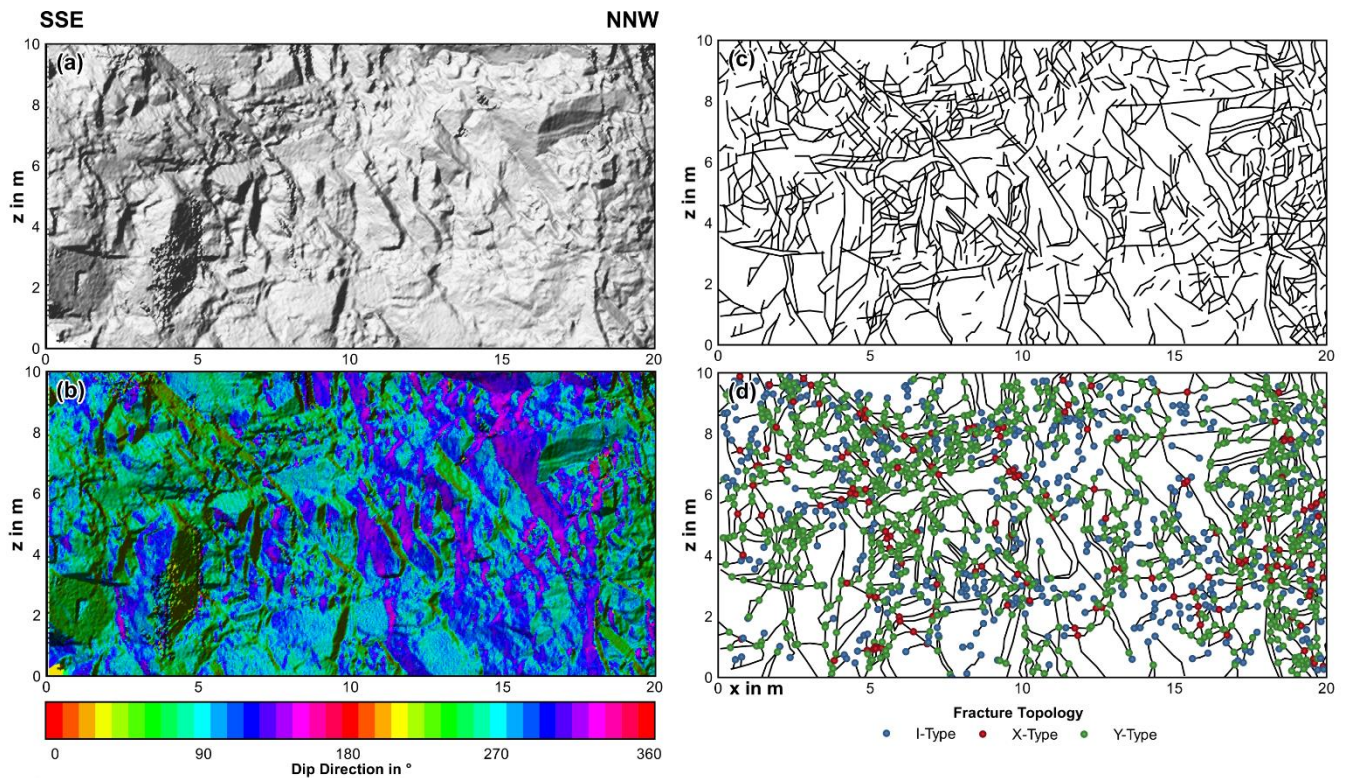
Figure 3: Interpretation of a scanned outcrop wall from the quarry in Ober-Mengelbach (Profile A in Fig. 2): (a) rasterized side view; (b) calculated dip direction; (c) manually interpreted fracture traces; (d) topology of the fracture nodes.

Besides the automatic plane recognition, the LiDAR data were also manually interpreted in QGis to investigate the fracture length, density and connectivity (Fig. 3). For this purpose, side projections of the point clouds were rasterized and hill shade maps were again generated. Visible fractures were then digitized to compute the fracture areal density P20 and intensity P21. Additionally, the linear fracture frequency P10 was extracted along virtual horizontal scanlines for each outcrop. The topology of the fractures was furthermore studied to characterize the connectivity of the network. For this, the tips of all fracture branches were classified into three groups: isolated (I), abutting (Y) and crossing (X) nodes. The average number of connections per line C_L was calculated from the number of nodes per type (Sanderson and Nixon, 2018).

The results of the lineament and outcrop analyses are finally summarized in a normalized trace length cumulative frequency plot with a power-law fitted to the data, which describes the relationship between frequency and the cumulative distribution of fractures lengths (Pickering et al., 1995; Marrett et al., 1999).

3.1.3 DFN modelling

DFN models were generated with the software FracMan to quantitatively model the hydraulic properties of the fractured crystalline basement based on the structural parameters acquired in the field. Fracture orientations were implemented by

8

175 performing a cluster analysis on the dip directions and dip angles extracted from the LiDAR data. The fracture density was defined along a virtual horizontal borehole using the calculated P10 values. The fracture length distribution was set according to the computed power law. A lower cut-off of 70 cm was applied, as significant censoring, i.e. under-representation of short fractures, occurs below this length. The effective fracture aperture largely governs the hydraulic conductivity of fractures. Due to exhumation and weathering processes, measured aperture values at near-surface outcrops are usually not reliable (Place et

180 al., 2016). Instead, an exponential distribution of the apertures and following Sausse and Genter (2005) three possible mean values (10 μm, 50 μm and 100 μm) were assumed. A more accurate approach would be to relate the aperture to the normal stress on the fracture plane (Bisdom et al., 2017), but as the local stress magnitudes are largely unconstrained in the Tromm Granite, this was not pursued further. Additionally, previous studies showed that a major part of the naturally occurring fractures in the crystalline basement are mineralized at reservoir depth and therefore only a small share of the fractures allow

185 fluid flow (Genter and Traineau, 1996; McCaffrey et al., 1999; Evans et al., 2005). For this reason, three different scenarios for the proportion of hydraulically active fractures in the DFN model were defined (1, 10 and 100%).

For a sufficient number of discontinuities, the fractured basement behaves like an anisotropic porous medium. The equivalent porous medium (EPM) permeability tensor can thus be calculated for a DFN model by, e.g., the approach of Oda (1985). The undisturbed rock matrix is considered impermeable (Jing and Stephansson, 2007; Weinert et al., 2020), implying that fluid

190 flow occurs exclusively through connected fractures. The directional permeability is related to the size, orientation, opening and connectivity of the fractures. One key factor is the relationship between fluid flow along a fracture and the aperture, described by a cubic law (Snow, 1965). This relationship is based on the assumption of laminar flow between two parallel surfaces, which is often not the case due to the irregular surface and aperture of the fractures and can therefore lead to errors. The permeability tensors were computed along a regularly spaced grid with a cell size of 10 m to reduce the computational

195 effort and afterwards, mean values were calculated for the entire DFN model. Different cell sizes between 1 m and 20 m were tested, revealing no significant differences in the resulting mean permeability tensor.

3.2 Geophysical surveys

3.2.1 Gravity data/survey

During two surveys in summer 2020 and spring 2021, gravity measurements at 431 stations along 11 profiles have been

200 conducted in the Tromm Granite (Fig. 2). Since a differential GPS was used to determine the position, the campaigns were restricted to the southern, less densely forested part. The GPS data were corrected against known fix points, resulting in c. 10 to 20 cm vertical accuracy. Gravity measurements were performed using the Scintrex® CG-6 Autograv gravimeter with an average station spacing of 100 m respectively 20 to 25 m close to presumed fault zones. Base measurements were taken three times per day at a fixed station to record the instrument drift. Measurements with a standard deviation greater than 0.05 mGal

205 were excluded. A complete Bouguer anomaly was calculated for all gravity stations by applying the standard correction density of 2,670 kg m⁻³, which corresponds approximately to the mean rock density of the Tromm Granite (Weinert et al., 2020), as

also confirmed by Nettleton analysis (Nettleton, 1939). Particular focus was on the topographic correction, which along some profiles reaches up to 2 mGal due to the steep terrain. The calculation was performed with the software GSolve (McCubbine et al., 2018) in three separate zones (Zone 1: 0 to 2.1 km, DEM 10 m; Zone 2: 2.1 to 81 km, DEM 100 m; Zone 3: 81 to 167 km, DEM 1 km). Taking into account all uncertainties in the data acquisition and processing, especially the height error and the standard deviation of the measurement, a cumulative error of the Bouguer anomaly of less than 0.1 mGal was determined. For the regional gravity signal analysis, c. 5300 additional data points provided by the Leibniz Institute for Applied Geophysics (LIAG) and the Hessian Administration for Land Management and Geoinformation (HVGB) were used within a radius of 50 km around the survey area. Together with the newly acquired data, a Bouguer anomaly map with a nominal resolution of 20 m was calculated using the minimum curvature interpolation method. A series of high-pass filters with cut-off wavelengths of 10 km, 5 km, and 2 km was then applied to subtract the regional gravity field.

3.2.2 Inversion of the gravity data

A stochastic 3D inversion of the high-pass filter Bouguer anomaly (10 km cut-off wavelength) was performed to infer the density distribution and the porosity in the subsurface. The commercial platform GeoModeller (Intrepid Geophysics) was used for this purpose, which employes a Monte-Carlo Markov-Chain algorithm to invert geophysical data. A detailed discussion of the methodology is available in previous studies (Guillen et al., 2008). The model domain has an extension of 7 km in E-W and 6 km in N-S direction and a depth of 2 km. The upper boundary is defined by the 10 m DEM. Given the relative homogeneity of the pluton with respect to the matrix density and the lack of structural input data, an unconstrained inversion was performed. The continuous model was converted into a discrete cuboid voxel model with a cell size of 50 x 50 x 50 m. Further decreasing the cell size potentially resolves more details but exponentially increases the computational time of the inversion. As starting value for the rock density, a mean density of the Tromm Granite of $2{,}670 \pm 50$ kg m^{-3} was defined (Weinert et al., 2020).

The algorithm first calculates the geophysical effect of the starting model, in this case a homogenous half-space, and then uses a Bayesian approach to determine the likelihood of the model. In subsequent iterations, random variations of the model are generated according to the probability distribution of the rock density. Models that lead to a reduction in the misfit between calculated and measured gravity anomalies have a higher likelihood and are stored. After 250 million iterations, a larger collection of possible models is generated, allowing statistic evaluation.

Finally, the porosity is estimated assuming the above mentioned homogeneity of the Tromm granite by

$$\Phi = \frac{\rho_{bulk} - \rho_{matrix}}{\rho_{fluid} - \rho_{matrix}} \tag{1}$$

Where ρ_{bulk} is the bulk density, ρ_{fluid} the fluid density (c. 1,000 kg m^{-3}), ρ_{matrix} the matrix density and Φ the porosity. Note that this equation can not simply be applied in the southernmost Tromm Granite, where significant lithological heterogeneity is observed, resulting in variations of the bulk density without the influence of increased fracture porosity.

3.2.3 Radon measurements

Radon is a naturally occurring radioactive gas that is concentrated in the soil air. The most abundant Rn-isotope with a proportion of c. 90 % is Rn-222 with a half-life of 3.82 days, formed in the decay series of U-238 . Permeable fault zones may provide migration pathways where Rn-222 transport to the surface is enhanced. Consequently, elevated radon concentrations are expected in the close vicinity of hydraulically active faults (Ioannides et al., 2003; Baskaran, 2016; Jolie et al., 2016; Vazaios et al., 2017).

Measurements of the activity concentration [Beq m^{-3}] of Rn-222 were carried out with the Saphymo AlphaGUARD 2000Pro at 20 points on one profile that crosses two presumed fault zones (Fig. 2b). Soil air was sampled using a hollow probe driven 1 m deep into the subsurface. A pump was connected to this probe, which flooded the ionization chamber of the radon monitor. The activity concentration was measured within 1-minute cycles. After 15 minutes, the air in the chamber was completely exchanged. The pump was then switched off, and the chamber short-circuited for an additional 10 minutes. During this time interval, most of the very short-lived Thoron (Rn-220, $t_{1/2}$ = 55.6 s) decayed so that the final reading corresponded only to Rn-222 concentration. Furthermore, soil samples were taken with a slotted probe at all stations to determine the soil type. Repeated measurements were performed at a base station to quantify the temporal variability of the concentration measurements.
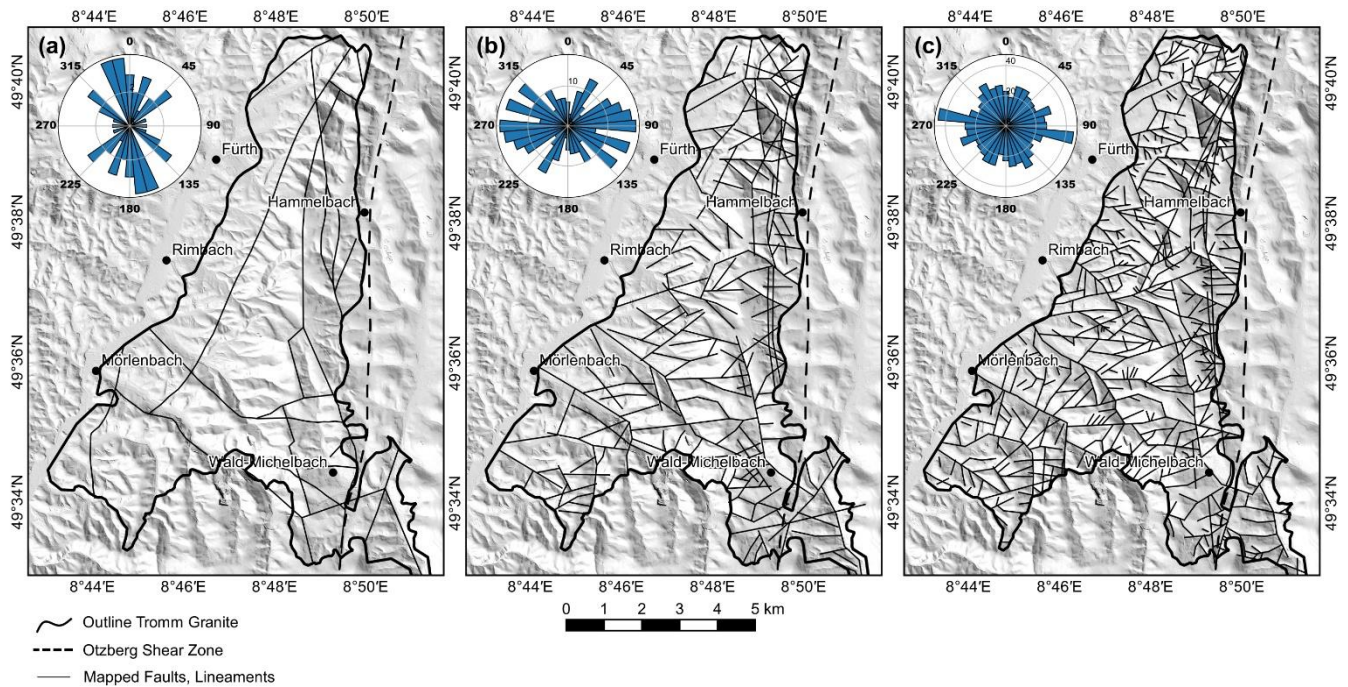
4 Results

4.1 Fracture network properties

4.1.1 Lineament distribution

Fig. 4 and Table 1 compare the faults that were determined by geological mapping in the Tromm Granite area with the geologically significant lineaments extracted from the SRTM model and the DEM with 1 m resolution. A total of 30 faults with a characteristic length (arithmetic mean of the fracture length) of c. 2,900 m were extracted from geological maps (modified after Klemm, 1900, 1928, 1929, 1933; HLUG, 2007), corresponding to a P21 value of 0.0014 m m^{-2}. The total number of elements that were identified with the lineament analyses is significantly higher (177 for SRTM and 471 for the 1m DEM). Their characteristic length of 1187 m and 680 m, respectively, is smaller and decreases with increasing resolution. The P21 is 0.0034 m m^{-2} for the SRTM lineaments and 0.0051 m m^{-2} for the lineaments of the high-resolution DEM. In all data sets, a heterogeneous spatial distribution of the faults or lineaments can be observed. The element density is highest in the eastern part of the Tromm Granite, i.e. in the area influenced by the Otzberg Shear Zone. The density is significantly lower in the west, especially for the mapped faults and the SRTM lineaments.

The main strike of the mapped faults ranges from 160° to 170°, which corresponds approximately to the direction of the maximum horizontal stress S_{Hmax} (Reiter et al., 2016). In contrast, the main set of SRTM lineaments strikes with 090 ±30°. The strike directions of lineaments from the high-resolution DEM show nearly an equal distribution, with a slight accumulation of lineaments at 100°.

Figure 4: Summary of the lineament analysis in the Tromm Granite area: (a) compilation of mapped faults from various geological maps (modified after Klemm, 1900, 1928, 1929, 1933; HLUG, 2007); (b) regional analysis using SRTM data with 1 arcsecond resolution (van Zyl, 2001); (c) local analysis using 1 m DEM provided by the HVBG.
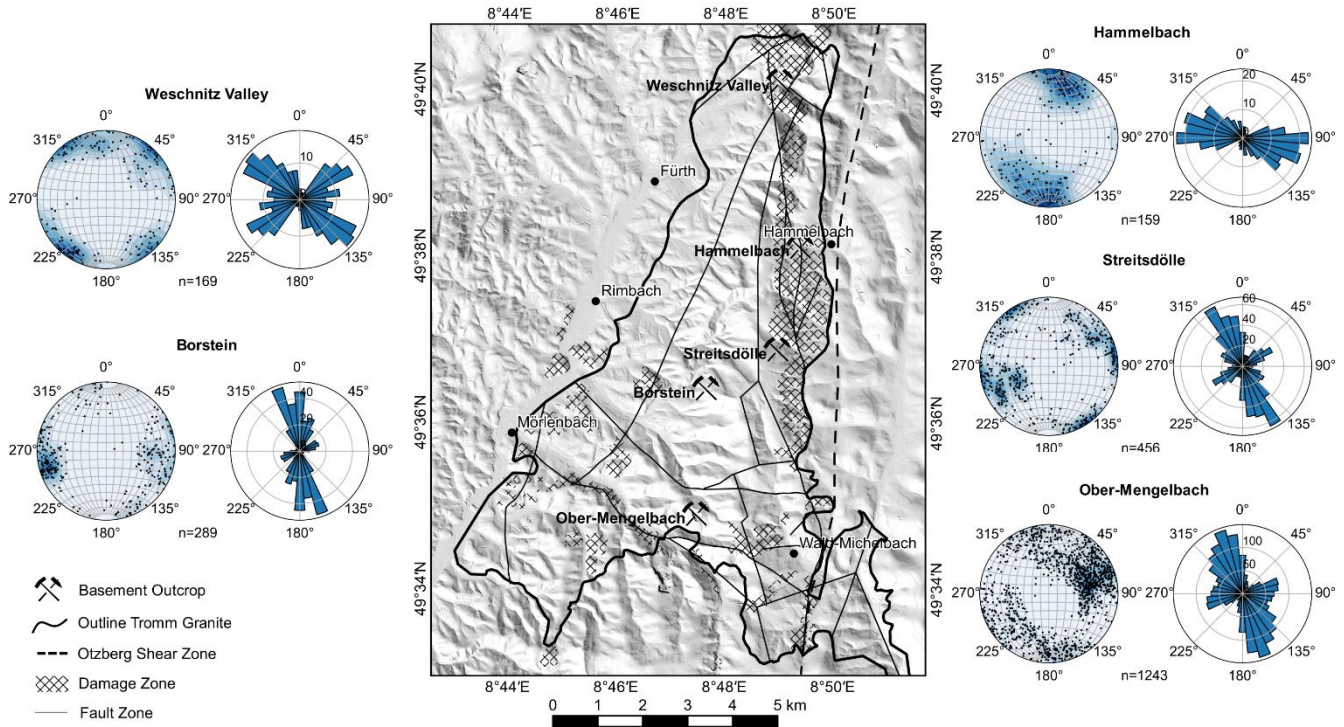
4.1.2 Fracture networks in outcrops

In total five outcrops of varying size, distributed over the entire Tromm Granite area and hence representing the heterogeneity of the pluton, were investigated using LiDAR (Figs. 1 and 2). Outcrop walls are generally vertical. The two abandoned quarries Borstein and Streitsdölle in the central part of the study area are dominated by the typical, medium- to coarse-grained Tromm Granite. Remnants or intrusions of other rock species are scarce, but veins of younger granites can frequently be observed. These two outcrops have the lowest areal fracture intensity with a P21 of 2.43 m m^{-2} and 2.83 m m^{-2}, respectively (Table 1). Conversely, the fracture characteristic length is the longest here, reaching 1.28 m and 1.62 m respectively. The main set of fractures dips steeply and strikes 160 ±20°, which corresponds to the main direction of the geologically mapped faults in the Tromm Granite (Fig. 4). A second, subordinate set of steeply dipping conjugate fractures strikes 060 ±10°. Shallow dipping fractures are very rare.

The most extended outcrop examined is an abandoned quarry with dimensions of c. 150 × 250 m close to the village of Ober-Mengelbach at the southern border of the Tromm Granite (Fig. 3). In contrast to Borstein and Streitsdölle, the lithological conditions found here are more heterogeneous. Meter- to ten-meter-wide amphibolite zones were observed throughout the quarry that are highly deformed and intruded by granite or granodiorite. The magmatic contacts are usually not abrupt but rather characterized by mixed forms of amphibolite and granitoids. Again, several generations of granite intrusions can be distinguished. The distribution of fractures was investigated along four 2D profiles with a length between 20 and 30 m, and a

height of 10 m (see Fig. 2 for location). The P21 ranges from 3.60 to 5.87 m m^{-2} and is thus about twice as high as in the central Tromm Granite. The extraction of fracture orientations using the Ransac filter was carried out for all outcrop walls to obtain the most comprehensive data set possible. Again, the primary set of fractures strikes 160 ±20° and a secondary set strikes 070 ±10° (Fig. 5).

The two smaller outcrops in Hammelbach and the Weschnitz valley are located at the northeastern border of the Tromm Granite. Here, a fine- to medium-grained, cataclastic granite is predominant, which was considerably affected by the adjacent Otzberg Shear Zone. Consequently, the P21 is the highest with 10.82 m m^{-2} and 9.07 m m^{-2}, respectively. The fracture orientation also differs significantly from the other three locations. In Hammelbach, the fractures strike almost exclusively 100 ±20°. In the Weschnitz Valley at the northern margin of the Tromm Granite, two fracture sets were found, striking 050 ±10° and 130 ±20°, respectively. These directions correlate well with the orientation of the close-by lineaments.

Figure 5: Summary of the outcrop analysis in the Tromm Granite area (faults and outline of the Tromm Granite from HLUG (2007) and Klemm (1900, 1928, 1929, 1933)).

13

Table 1: Summary of fracture network properties for all outcrop analyzed in the Tromm Granite area. OMB = Ober-Mengelbach.

Object	Area [m²]	No. fractures	Min. length [m]	Max. length [m]	Char. length [m]	P10 [frac. m⁻¹]	P10 > 70 cm [frac. m⁻¹]	P20 [frac. m⁻²]	P21 [m m⁻²]	c_L
Faults & Lineaments										
Fault compilation	$62.7 \cdot 10^6$	30	195	9,369	2,899	-	-	$4.79 \cdot 10^{-7}$	0.0014	-
SRTM (1 arcsecond)	$62.7 \cdot 10^6$	177	238	4,624	1,187	-	-	$2.84 \cdot 10^{-6}$	0.0034	-
DEM 1m	$62.7 \cdot 10^6$	471	74	9,001	680	-	-	$7.53 \cdot 10^{-6}$	0.0051	-
Outcrops										
Borstein	475	903	0.10	11.22	1.28	1.62	1.31	1.90	2.43	2.96
Hammelbach	67	1351	0.03	3.91	0.54	6.95	2.27	20.16	10.82	3.94
Streitsdölle	288	521	0.06	12.96	1.57	1.90	1.61	1.81	2.83	3.44
Weschnitz Valley	119	1,332	0.03	7.57	0.81	7.05	4.25	11.19	9.07	4.09
OMB total	1,050	5,778	0.02	10.28	0.83	2.66	1.69	5.50	4.54	3.23
OMB Profile A	200	767	0.05	7.27	0.98	2.73	1.84	3.84	3.78	3.02
OMB Profile B	300	1647	0.06	6.24	0.89	3.17	2.07	5.49	4.89	3.11
OMB Profile C	250	2,383	0.02	7.74	0.62	3.42	1.65	9.53	5.87	3.30
OMB Profile D	300	981	0.06	10.28	1.10	2.34	1.59	3.27	3.60	3.43

4.1.3 Length distribution and fracture connectivity

305 Fig. 6a provides a compilation of all identified faults and geologically significant lineaments from the Tromm Granite, with the length plotted against the cumulative number of fractures normalized to the analyzed surface area. Length values range from 0.02 m to 9 km, hence covering about six orders of magnitude. The data points follow a power-law distribution with an exponent of -1.96, which represents a typical value for fracture networks in the crystalline and especially granitic basement, as shown in previous studies (Bertrand et al., 2015; Bossennec et al., 2021; Chabani et al., 2021). Deviations of the lineament

310 and fracture data from this law can be explained by censoring and truncation effects. While not all small-sized fractures can be identified due to the limited resolution of the LiDAR point clouds, the full length of long fractures is often truncated at the edges of the visible outcrop walls. To obtain the best power-law fit, a lower cut-off length of 70 cm for the outcrop fractures and 500 m for the lineaments was therefore selected.

The IXY-topology was examined to quantify the connectivity of the encountered fracture networks, expressed by the average

315 number of connections per line c_L. An interpretation was made for the fractures on the outcrop scale and the lineaments on the regional scale (Fig. 6b). All datasets plot in the lower-left corner of the IXY diagram, showing a dominance of Y-nodes. The proportion of I- and X-nodes ranges from 5 to 15 %, respectively. This node topology results in a c_L of c. 3 to 5, indicating generally high connectivity of the fractures. Besides, a correlation between fracture intensity and connectivity can be seen.

The lowest c_L (2.96) was determined for the Borstein outcrop, where P21 is also the smallest (2.43). In Hammelbach and in the Weschnitz Valley, the highest P21 (c. 9 - 11 m m^{-2}) and c_L (c. 4) values were found. Another striking feature is the high connectivity of the mapped faults, exhibiting almost no isolated ends, which might result from a bias of the mapping geologist.
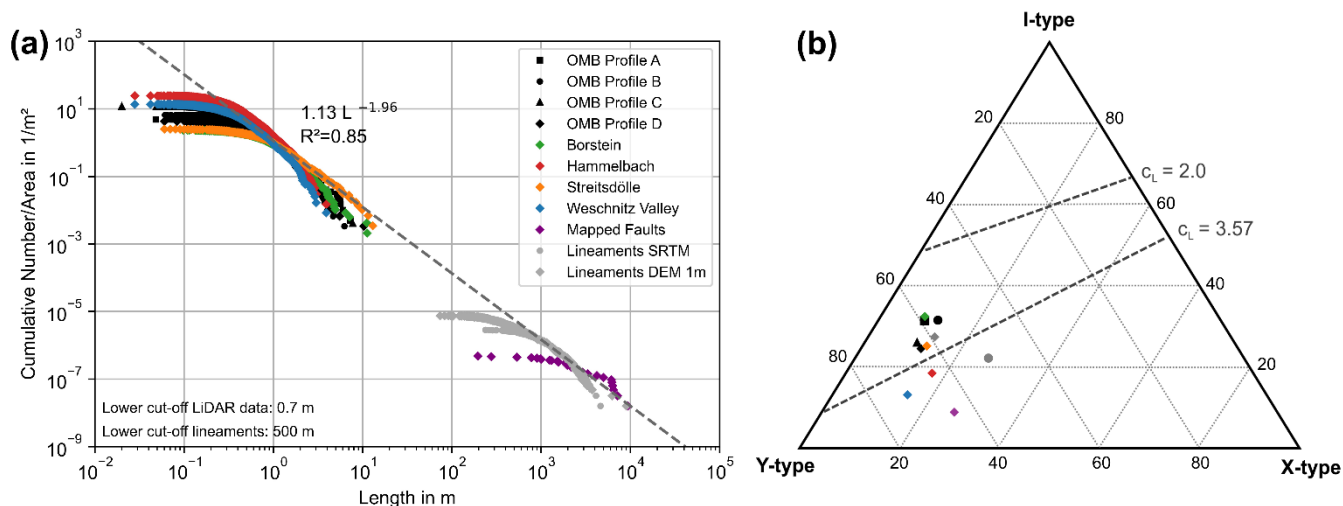
Figure 6: (a) Area-normalized trace length cumulative frequency plot; (b) triangular plot of the proportion of I-, X- and Y-nodes of the analyzed outcrops.
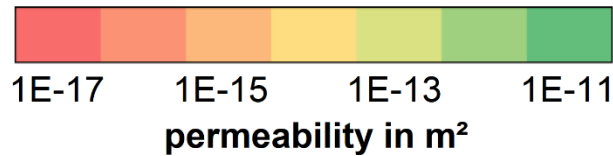
4.1.4 Results of DFN modelling

DFN models were created for the two outcrops Borstein and Weschnitz Valley, representing the end members of the Tromm Granite in terms of fracture density (Fig. 7). The estimated EPM permeabilities in x- (E-W-), y- (N-S-) and z-direction are summarized in Fig. 8. The fracture mean aperture has the largest influence on the permeability, as these two parameters are related via a cubic law. Practically speaking, this means that increasing the aperture by one order of magnitude leads to three orders of magnitude higher permeability. The proportion of open fracture, in contrast, is linearly related to permeability, i.e. a tenfold increase also increases permeability by a factor of ten. The orientation of the fracture sets has furthermore a significant effect on the permeability of the basement. At Borstein, the permeability in the main direction of the fractures (k_{yy}) is almost one order of magnitude higher than perpendicular to it (k_{xx}). Finally, the difference between Borstein and Weschnitz Valley reaches again up to one order of magnitude, depending on the direction, for the same aperture and proportion of open fractures. This variability is mainly due to approximately four times higher fracture density in the second outcrop (Table 1).

15
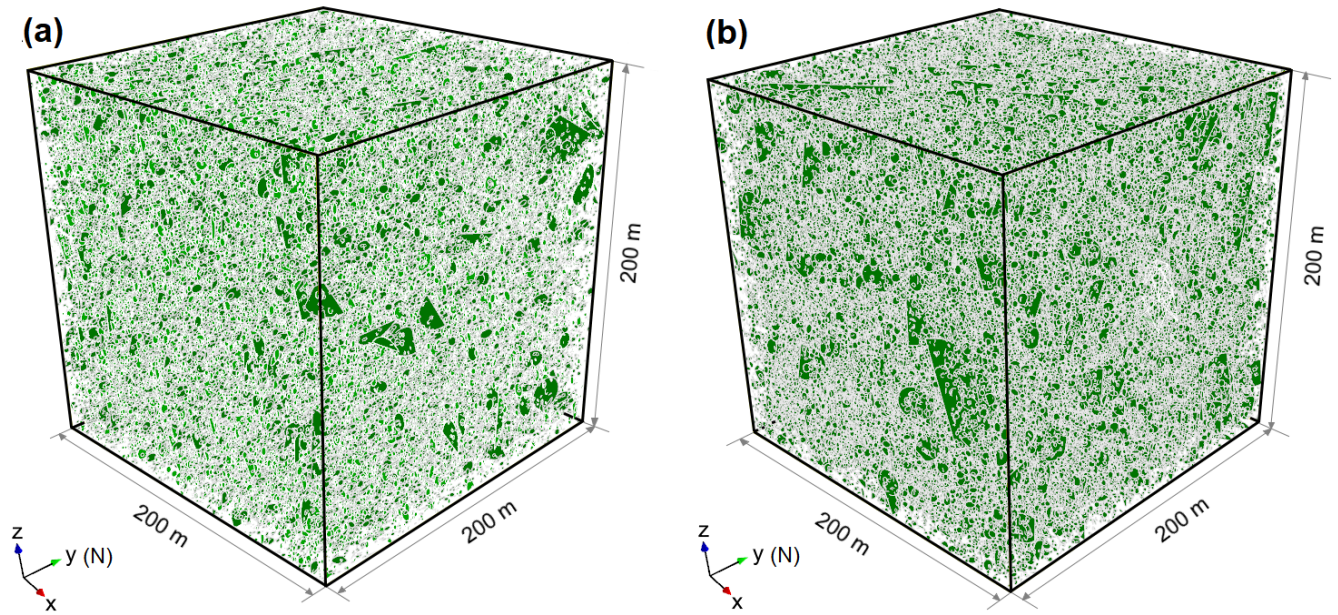
Figure 7: Illustration of DFN models with 1 % open fractures for (a) the Borstein quarry (n = 214287) and (b) the Weschnitz Vally quarry (n = 279787).

		Borstein			Weschnitz Valley		
		mean aperture			mean aperture		
	m²	10 μm	50 μm	100 μm	10 μm	50 μm	100 μm
100% open	k_{xx}	5.0E-16	6.3E-14	5.0E-13	3.8E-15	5.1E-13	4.1E-12
100% open	k_{yy}	2.1E-15	2.5E-13	1.9E-12	1.7E-15	2.2E-13	1.7E-12
100% open	k_{zz}	2.2E-15	2.6E-13	2.0E-12	4.5E-15	6.0E-13	4.7E-12
10 % open	k_{xx}	4.8E-17	6.2E-15	4.9E-14	4.0E-16	5.6E-14	3.4E-13
10 % open	k_{yy}	2.0E-16	2.5E-14	1.9E-13	1.7E-16	2.3E-14	1.5E-13
10 % open	k_{zz}	2.1E-16	2.6E-14	2.0E-13	4.7E-16	6.5E-14	4.0E-13
1 % open	k_{xx}	7.6E-18	1.9E-15	1.1E-14	5.2E-17	1.2E-14	5.7E-14
1 % open	k_{yy}	2.6E-17	3.2E-15	5.1E-14	2.6E-17	5.2E-15	2.5E-14
1 % open	k_{zz}	2.7E-17	4.4E-15	5.1E-14	6.6E-17	1.4E-14	6.7E-14

1E-17   1E-15   1E-13   1E-11

permeability in m²

Figure 8: Summary of the DFN modelling. The Oda permeabilities in x-, y- and -direction were calculated as a function of fracture density, orientation, aperture and proportion of open fractures.

To test the transferability of the results to crystalline reservoirs in the URG, a comparison with hydrogeological data e.g. from Soultz-sous-Forêts is useful. Here, the mean permeabilities of the fractured granitic basement range from 1E-16 to 1E-14 m² at reservoir depth of 3 to 5 km (Vogt et al., 2012; Baujard et al., 2017; Egert et al., 2020). Accordingly, realistic permeabilities result for (1) a mean aperture of 10 μm and (2) for 50 μm when 1 to 10 % of the fractures are open. For 100 μm, the calculated permeabilities are too high in all cases and would thus rather represent permeabilities of single large-scale fractures or faults, while the smaller scale fractures would have smaller fracture apertures.

It should be noted that the hydraulic properties of fractured reservoirs are subject to strong spatial variations. For example, permeability can be increased by several orders of magnitudes close to active faults. In contrast, at larger distance from these faults or large-scale fractures, the mean permeability of the basement is rather in the order of 1E-18 to 1E-17 m².

4.2 Gravity and Radon Anomalies

4.2.1 Bouguer anomalies

Fig. 9 integrates the results of the two gravity surveys into the existing datasets (© Leibniz-Institut für Angewandte Geophysik,
355 © Hessische Verwaltung für Bodenmanagement und Geoinformation). Within the Tromm Granite, Bouguer anomalies range from c. -10 to -5 mGal and are uncorrelated with topography. The gravity field in this area is dominated by an NW-SE oriented regional trend (Fig. 9b) that was obtained by applying a low-pass filter with a cut-off wavelength of 10 km. Residual anomalies involving presumably lower depth ranges were obtained by applying high-pass filters with decreasing cut-off wavelengths from 10 to 2 km (Fig. 9c-e). The residual field exhibits distinct positive and negative anomalies. However, especially in the
360 central part of the Tromm Granite, the lack of data points leads to considerable uncertainties.

The strongest positive anomaly of 1 to 1.5 mGal is located north of Wald-Michelbach and coincides with a major lineament. Similarly, a positive anomaly of 0.5 to 1 mGal can be observed along the presumed fault zone between Zotzenbach and Wald-Michelbach. The strongest negative anomaly with an amplitude of c. -0.5 to -1 mGal extends over several kilometres from SSW to NNE at the western boundary of the Tromm Granite to the Weschnitz Granodiorite. Note that this area is covered by
365 locally more than 20 m but generally less than 10 m thick Quaternary sediments. However, the anomaly increases and persists with increasing cut-off wavelength. Another negative anomaly of c. -0.4 mGal is located at the eastern boundary of the pluton, southeast of the village of Tromm. Here, the granite is highly fractured due to the proximity to the Otzberg Shear Zone, which is also indicated by the high concentration of local lineaments. However, a direct correlation between Bouguer anomalies and individual faults or lineaments is usually not observed.
370 Besides these larger anomalies, short-wavelength variations of the gravity signal in the range of -0.3 to 0.3 mGal occur on individual profiles, which is still significantly higher than the cumulative uncertainty of the Bouguer anomaly.

18
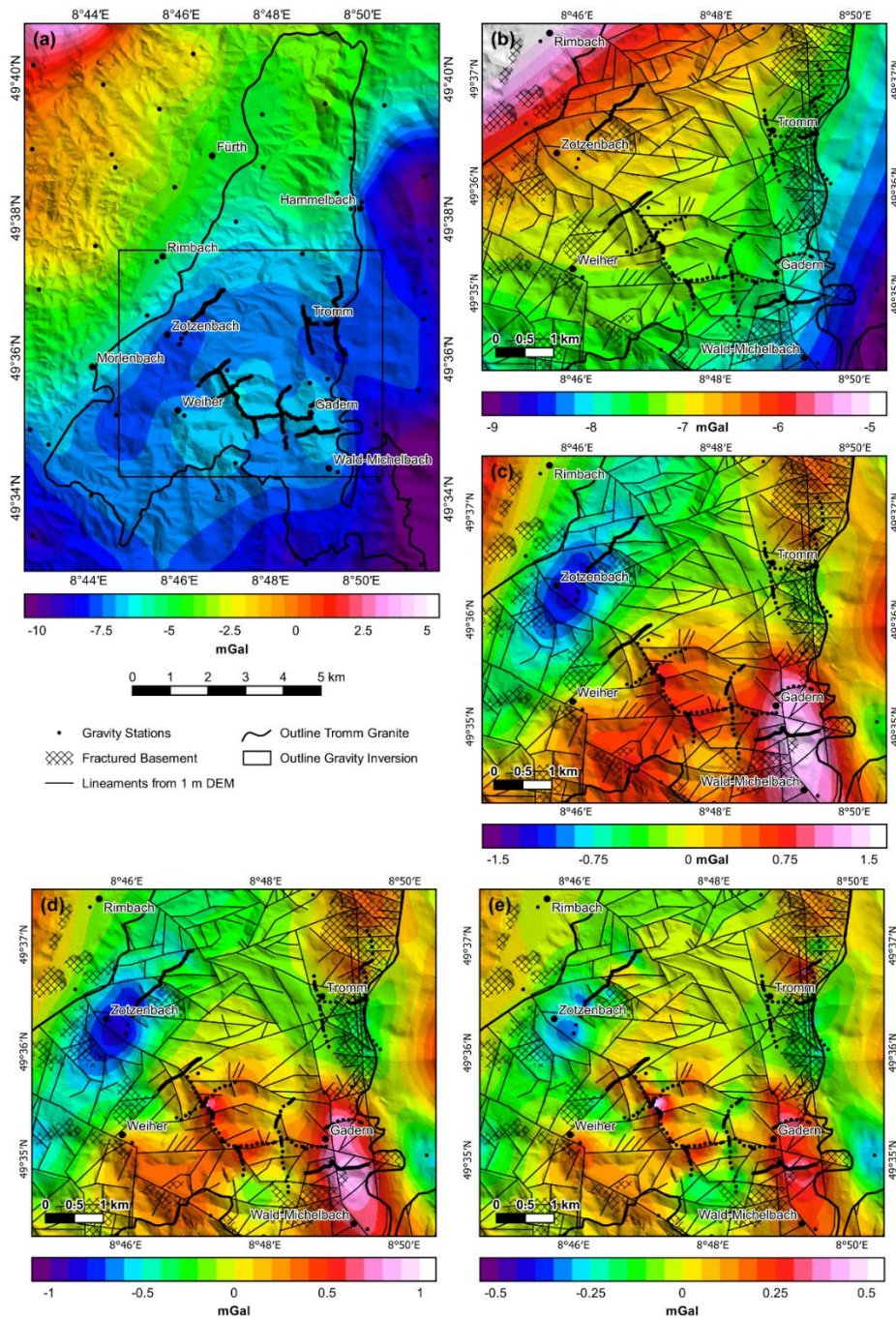
Figure 9: Results of the gravity survey: (a) Complete Bouguer anomaly map for the Tromm Granite (© Leibniz-Institut für Angewandte Geophysik, © Hessische Verwaltung für Bodenmanagement und Geoinformation); (b) low-pass filtered Bouguer anomaly with 10 km cut-off wavelength; (c) high-pass filtered Bouguer anomaly with 10 km cut-off; (d) high-pass filtered Bouguer anomaly with 5 km cut-off; (e) high-pass filtered Bouguer anomaly with 2 km cut-off.

4.2.2 Inversion results
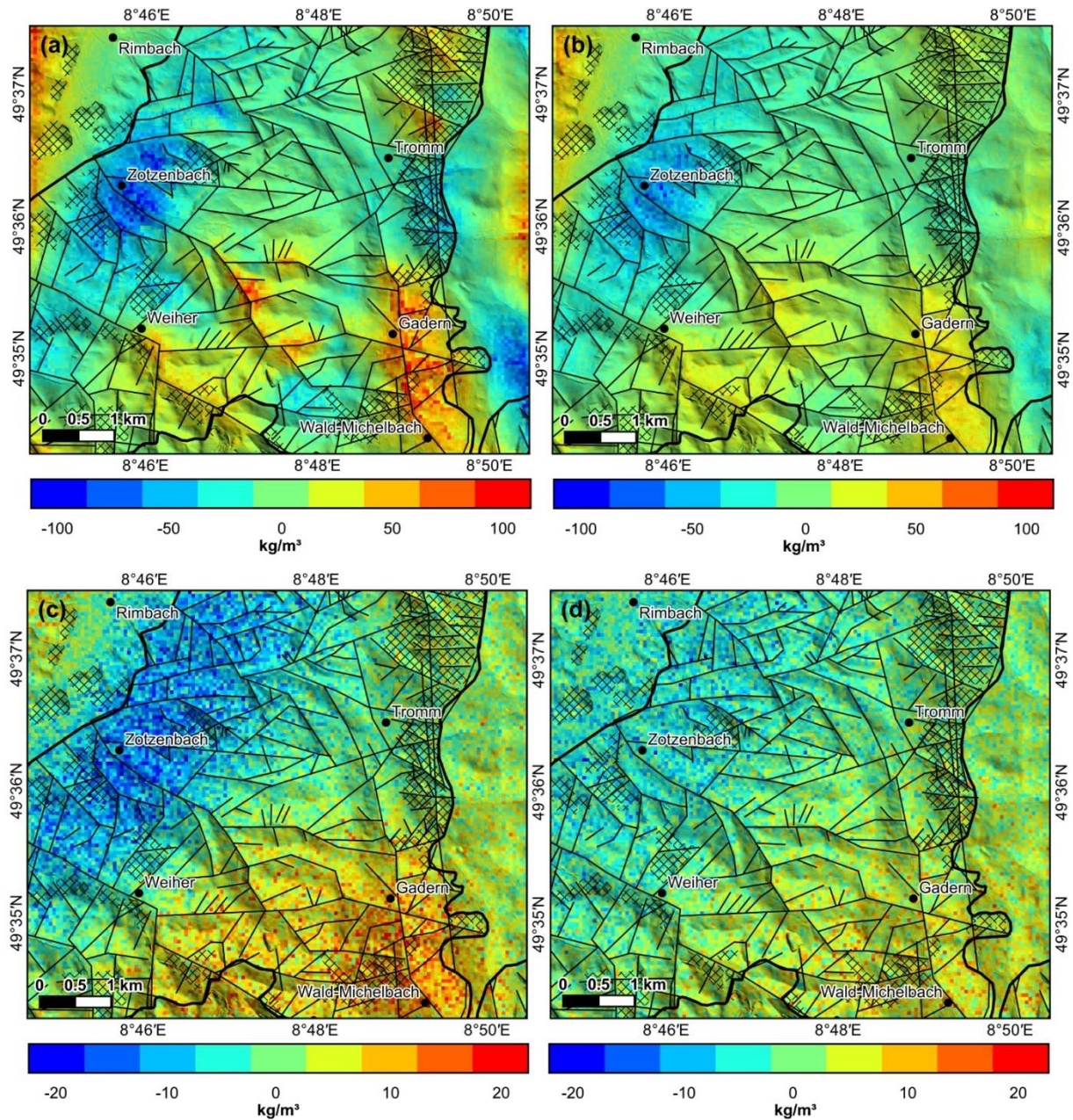
Figure 10: Results of the gravity inversion. Difference between inverted and initial density of 2,670 ± 50 kg m⁻³ at (a) the top of the basement, (b) 0 m a.s.l., (c) 1,000 m b.s.l. and (d) 2,000 m b.s.l. Be aware of the different colour scales for (a) and (b) vs. (c) and (d).

Results of the stochastic gravity inversion are shown as differences to the homogenous density of $2{,}670 \pm 50$ kg m⁻³ of the starting model in Fig. 10. The inverted mean densities range from 2,520 to 2,840 kg m⁻³ with an mean standard deviation of 2.5 kg m⁻³. Near the surface, the density distribution largely resembles the observed Bouguer anomalies. The most significant

20

density decrease of c. 100 kg m^{-3} is found at the western boundary of the Tromm Granite and may partly be related to the Quaternary cover. This difference decreases to about 50-75 kg m^{-3} below a depth of about 200 m. In addition, smaller density decreases in the range of 30 to 100 kg m^{-3} occur at the eastern boundary near the Otzberg Shear Zone. This area has been geologically mapped and attributed to the damage zone of the Otzberg Shear Zone. Assuming a lithological homogeneity of the Tromm Granite, this decrease would result in a fracture porosity of c. 2 to 6 %. Increased densities are mainly found in the area of the granodioritic Weschnitz Pluton and along the assumed fault in Gadern, north of Wald-Michelbach. Besides, very small-scale density variations are present in the south, which can be attributed to the lithological heterogeneity at the transition from Tromm Granite to the Schollenagglomerat Zone.

At greater depths, the inverted density model becomes more diffuse and the density variations are generally smaller. At 0 m a.s.l., the negative anomaly in the west and the positive anomaly in Gadern can still be clearly recognized. In contrast, the density reduction at the eastern edge is very weak. At 1,000 m b.s.l., the variations have a very long wavelength and only range between -30 and 30 kg m^{-3}. At the model base in 2,000 m b.s.l., the density is almost homogeneously distributed.

4.2.3 Comparison of gravity and radon measurements

A comparison of the radon activity concentration in soil air with the corresponding Bouguer anomalies is shown in Fig. 11 (see Fig. 2 for the location of the stations). A background activity of c. 25 kBeq m^{-3} was determined. The repeated base measurements furthermore revealed a standard deviation of 5 kBeq m^{-3}. Near the two assumed fault zones, a significant increase in the activity concentration can be observed with two pronounced peaks of 5 to 7 times the background value. The highest radon activity was measured in the zone between the two presumed faults (centre of Fig. 11) which coincides with a local negative Bouguer anomaly of c. -0.1 mGal, indicating an increase in fracture intensity and open porosity. The second peak is located close to the northeastern fault zone, but here, as with the southwestern fault, a positive Bouguer anomaly is present. Thus, there is only a partial correlation between the two data sets.
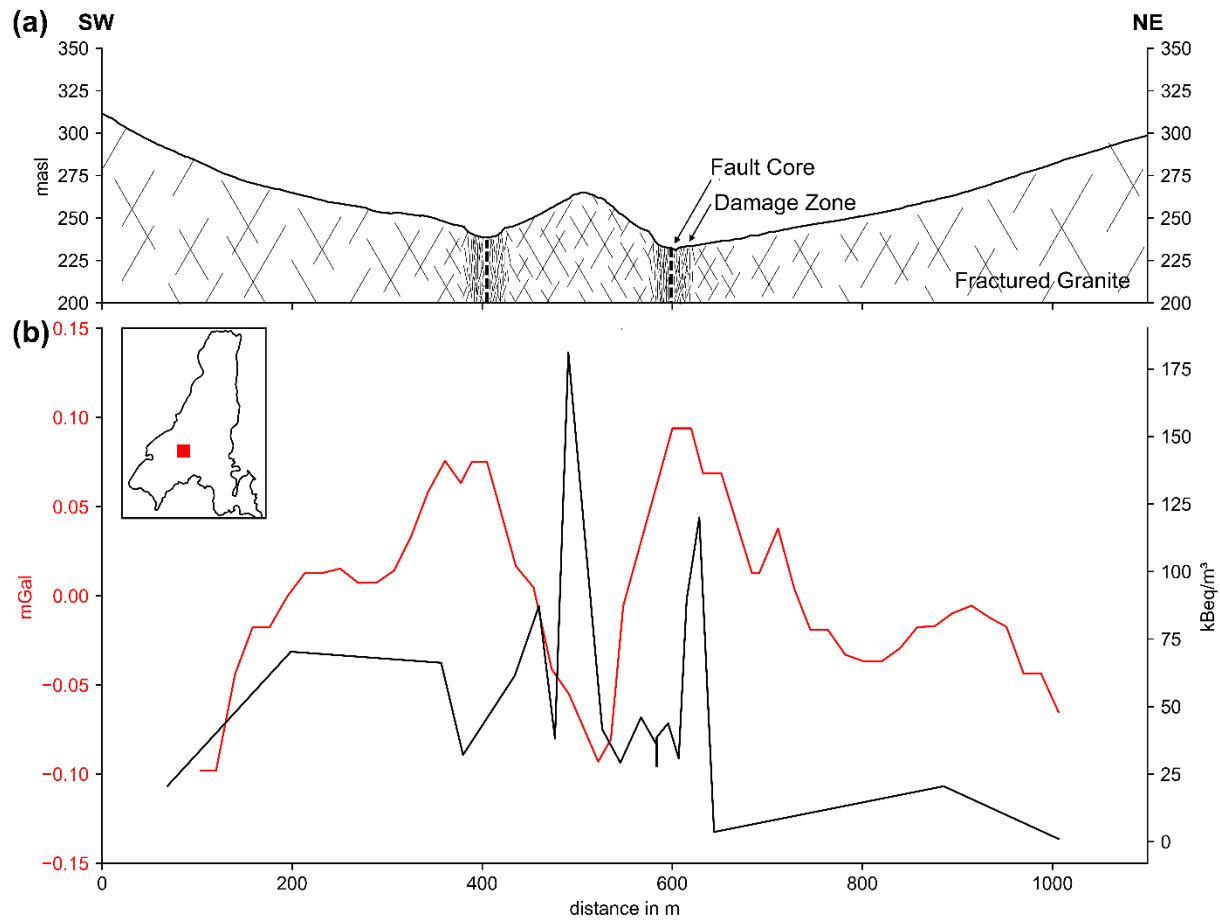
Figure 11: (a) Schematic cross-section of the investigated profile; **(b)** Comparison of the high pass filtered Bouguer anomalies (red line) and measured radon concentration in the soil air (black line).The small map shows the location of the profile within the Tromm Granite (see also Fig. 2).

5 Discussion

5.1 Fracture network characteristics

Based on the extensive structural geological investigations at the five outcrops and the lineament analysis, a more comprehensive description of the fracture network in the Tromm Granite has been obtained. Scale independence of fracture length distribution was demonstrated with a power-law exponent of c. -2. The length distribution is thus similar to other granitoid bodies in the URG region and other regions worldwide (Bertrand et al., 2015; Chabani et al., 2021).

Like the fracture length, the connectivity of the fracture network seems to be independent of scale or location. All outcrops and lineament maps indicate a dominance of Y-nodes, which is in clear contrast to the northern Odenwald, where I- and X-nodes represent the largest share (Bossennec et al. 2021). This can be attributed to different regional tectonic conditions during the intrusion, cooling and exhumation, or to overprinting under variable stress conditions.

22

420 Compared to fracture length and connectivity, the orientation of the fracture sets shows some scale-dependent and spatial variations. In the outcrops Ober-Mengelbach, Borstein and Streitsdölle, the fracture orientations are controlled by the main fault direction of 160 ±20° in the Tromm Granite. In contrast, the fracture sets of the two outcrops Hammelbach and Weschnitz Valley are more influenced by local fault zones, as indicated by the lineament analysis (Fig. 4). Furthermore, the N-S trend of the mapped faults can hardly be found in the two lineament maps. Instead, elements perpendicular to it, i.e. oriented E-W, are

425 dominant here.

Similar to the fracture orientation, the fracture density is subject to considerable lateral changes, which can be attributed to the influence of large-scale tectonic structures, especially at the pluton margins. In the eastern part of the Tromm Granite, the basement is deformed by the nearby Otzerg Shear Zone. As a result, there is an evident accumulation of lineaments and the outcrops show by far the highest fracture density. Medium fracture densities were found in Ober-Mengelbach, in the southern

430 part of the pluton, i.e. at the border to the Schollenagglomerat. Although this area lacks pronounced long fault zones, the lithological heterogeneities led to a more intense granite deformation than in the central Tromm Granite. Accordingly, the lowest fracture density was found in the outcrops Borstein and Streitsdölle.

In summary, the Tromm Granite is likely not characterized by a complete fractal fracture network, which is consistent, e.g., with studies from the western rift shoulder (Bertrand et al., 2018). Although fracture length and connectivity seem to be

435 independent of scale and location, orientation and fracture density show variations with location. This fact must be considered when evaluating and modelling the basement, as varying fracture orientation and density can increase or decrease permeability by up to one order of magnitude depending on the assumed mean apertures (Fig. 8).

5.2 Interpretation of gravity and radon anomalies

The measured gravity anomalies provide insights into the subsurface density distribution of the Tromm Granite (Fig. 10).

440 Negative anomalies of up to 1 mGal are concentrated at the western and eastern boundary of the pluton, where the basement is strongly deformed and fractured. Comparable results in the Argentera Massif (NW Italy) were linked to a few percent of fracture porosity (Guglielmetti et al., 2013). However, several tens of meters thick layer of low-density Quaternary sediments or a thick basement weathering horizon could also lead to negative gravity anomalies. Borehole data from the HLNUG suggest that Quaternary sediment thicknesses typically do not exceed 10 to 15 m, accounting for a maximum of -0.2 mGal of the signal.

445 Nevertheless, it is known that the weathering zone in the granite is locally 20 to 40 m thick, which could account for a gravity anomaly of up to -0.5 mGal.

In general, individual faults can rarely be accurately traced with the acquired gravity data in the Tromm Granite, as the influence of fracture porosity on bulk density is too small. Instead, areas can be identified where a high density of faults and fractures lead to increased porosity and thus to significant density reduction. Accordingly, the Tromm Granite is potentially

450 structurally weakened at the contact with the Weschnitz Pluton in the western part of the study area. Unfortunately, there are neither larger outcrops nor well data available, leaving this assumption speculative. The slightly smaller negative anomaly at the eastern boundary to the Buntsandstein can be explained by the proximity to the Otzberg Shear Zone. Here, the pluton is

23

presumably characterized by similar structural properties as in the Hammelbach, and Weschnitztal outcrops, which means that the fracture density and thus the porosity are increased. Interestingly, the anomaly does not extend over the entire damage zone at the eastern margin of the Tromm Granite but is concentrated in a limited area with a high density of intersecting lineaments. A possible explanation is that the fractures are partially mineralized with e.g. barite (e.g. Tranter et al., 2021), resulting in increased bulk density.

Positive gravity anomalies of up to 1.5 mGal can be observed at the southern Tromm Granite along two fault zones. In Gadern, several lamphropyric intrusions were mapped and, as in the quarry of Ober-Mengelbach, localized amphibolitic zones are present. These mafic rocks have a considerably higher density (2700 – 3100 kg/m³) than the Tromm Granite, which explains the gravity high. Due to the lithological heterogeneity in the southern Tromm Granite, quantification of fracture porosity using the gravity data is difficult here.

Radon measurements were carried out along just one profile due to the high time consumption of this method. Accordingly, a regional interpretation of the results is only possible to a limited extent. Nevertheless, the determined radon anomalies give helpful indications about the architecture of the analyzed fault zones. Two distinct radon peaks indicate localized permeable fracture zones in the granite. The highest activity correlates with a negative Bouguer anomaly which further supports this assumption. Interestingly, the peaks are not located directly above the assumed position of the faults, but in the damage zone a few metres to tens of metres to the sides, suggesting low permeability in the fault core (Caine et al., 1996). The comparison of gravity, radon and structural data illustrates the complex architecture of fault zones in the crystalline basement (Bossennec et al., 2021; Faulkner et al., 2010; Bossennec et al., 2022), consisting of several adjacent permeable and impermeable zones, which may also be influenced by clay mineralization. By combining gravity and magnetic field data, it is thus possible to study on the one hand the dimensions of the fracture network, and on the other hand to evaluate its behavior (sealed or open).

5.3 Implication for GeoLaB and deep geothermal exploration

The Tromm Granite represents a suitable site for the planned geothermal underground research laboratory (GeoLaB), as the main criteria proposed by Schill et al. (2016) are met. Firstly, except for the southern part, the pluton exhibits low geological complexity with a rather homogeneous crystalline matrix. The high fracture density of 1.62 to 6.95 m⁻¹ and good connectivity ensures sufficient hydraulic fracture permeability for the experiments. As required, the Tromm Granite is located in a normal faulting to strike-slip regime. In addition, the primarily NNW-SSE oriented fractures have a high reactivation potential in the ambient stress system. There is no extensive drainage in the area due to historical mining activities in adits, resulting in controllable hydraulic boundary conditions. Finally, the topography in the central part of the Tromm Granite can be described as plateau-like, allowing an overburden of the tunnel between 300 and 400 m, which assures undisturbed stress conditions. The interdisciplinary data set described herein will serve as an important basis for the planning of further exploration activities in the area as well as the final site selection.

Furthermore, the Tromm Granite is a well-suited outcrop analogue for the crystalline basement in the URG. The granitic body has a similar mineralogical composition as the reservoir rocks e.g. in Soultz-sous-Forêts or Rittershoffen (Dezayes et al.,

2005b; Traineau et al., 1991; Vidal et al., 2018). Granitoids are dominant in the northern URG, as inferred from the joint inversion of gravity and magnetics data (Frey et al., 2021a; Baillieux et al., 2013). Moreover, the Tromm Granite was intruded in the same tectonic setting and overprinted under comparable conditions as the granites of the URG. Nevertheless, a direct transfer to deep geothermal reservoirs, where in-situ hydrothermal alteration and mineralization as well as complex geomechanical processes occur, is challenging considering that weathering and exhumation significantly affect the near-surface fracture network. Unfortunately, no major fault zone is exposed in the study area, making it virtually impossible to evaluate the true nature of mineralization and fluid circulation patterns. The applied gravity and radon surveys help to overcome this lack of outcrops and provide insights into the basement's permeability structure.

A DFN parameter study was carried out to estimate the hydraulic properties of the Tromm Granite under assumed reservoir conditions (Fig. 8). The calculated permeabilities show a range of several orders of magnitude, indicating the uncertainties of this approach. Direct transfer of the hydrogeological properties to the reservoirs is therefore only possible to a limited extent, but the effect of individual parameters can be well followed. The fracture aperture primarily determines the permeability of the basement, which is in agreement with detailed sensitivity studies, e.g. performed by Niven and Deutsch (2009) or Mahmoodpour et al. (in review). The degree of mineralization (here considered as the proportion of open fractures), the fracture density, and the fracture orientation also influence the Oda permeability, but have a smaller effect. DFN modelling suggests that only a small proportion of the total fracture network is contributing to flow. With an average aperture of 10 to 50 μm, probably only 1 to 10 % of the fractures allow fluid flow, which fits well with observations from Soultz-sous-Forets (Egert et al., 2020; Sausse et al., 2010). It should also be noted that k_{xx} and k_{yy} show a difference of up to one order of magnitude (e.g. Mahmoodpour et al., 2021), which is particularly relevant for planning the well path trajectories of geothermal doublets and the experiments in GeoLaB. Accordingly, a geothermal doublet oriented approximately in a direction, that the open-hole sections intersect a high number of N-S oriented fractures probably yields the highest production rates, which is consistent with observations e.g. from Rittershoffen.

Minimizing induced seismicity during stimulation and operation represents a major challenge for deep geothermal exploitation of the crystalline basement (Rathnaweera et al., 2020; Zhang et al., 2013; Meller and Ledésert, 2017), and will be addressed experimentally in GeoLaB. Stimulation is generally more feasible in reservoirs with naturally elevated permeability, because lower injection pressures are required. The highest permeability is expected near large-scale fault zones with well-developed damage zones and hydrothermal overprinting. However, the structural geological investigations in Tromm Granite show that in certain areas sufficient permeability may also occur in the outer damage zones of large faults, i.e. at a distance of several hundred meters to kilometers from the fault core.

Besides hydrogeological properties, the temperature of the reservoir is an important parameter for any geothermal prospection. The thermal field in the URG has been extensively studied in the past (Pribnow and Schellschmidt, 2000; Bächler et al., 2003; Baillieux et al., 2013). Accordingly, temperature anomalies are mainly linked to hydrothermal convection zones, which cannot be localized very precisely using classical exploration methods so far. Bär et al. (2021) therefore propose an integrated

approach that combines 3D seismic, electromagnetic and gravity data with geothermal gradients from medium-depth boreholes, enabling more accurate mapping of ascending hot brines.

In addition to deep EGS projects, underground heat storage will significantly contribute to reduce emissions in the future energy supply. Thereby, seasonal fluctuations of other renewable energy such as solar and wind energy can be compensated. It is expected that medium depth borehole heat exchangers (MD-BHE) in the crystalline basement have the highest efficiency among comparable technologies and can be applied almost everywhere where the basement is situated near the surface (Welsch et al., 2016). Again, a detailed characterization of the fracture network is essential since open fractures can act as potential fluid conduits that reduce the heat recoverability. In this respect, the presented data can serve as input for thermal-hydraulic-mechanical simulations of MD-BHE to be built in the extended URG region.

6 Conclusions

The fracture network characterization of the Tromm Granite has led to the following conclusions:

- Combining outcrop and lineament analysis allows for a more comprehensive description of the main fracture network characteristics.

- While fracture length distribution and connectivity are mostly scale-independent, fracture orientation and density vary significantly across the Tromm Granite. The latter two parameters are heavily affected by the crustal-scale Otzberg Shear Zone.

- Hydraulic properties of the fractured basement under reservoir conditions can be estimated with DFN models and validated by hydraulic test data from deep boreholes. However, the calculated permeabilities are associated with large uncertainties, as the stress conditions and, therefore, the fracture aperture are highly unconstrained.

- Gravity and radon measurements enable a more advanced mapping of potentially permeable zones. The fracture porosity can be inferred from the inverted density model, where homogeneous subsurface conditions are present. Lithological variations and mineralization prevent exact porosity quantification.

- Structural investigations and gravity anomalies show that the most suitable hydraulic properties are expected at the margin of the granitic pluton, where regional-scale fault zones influence the fracture network. Moreover, during the cooling of a granitic pluton, the margins were more affected by the circulations of residual fluids and are therefore more altered than the center, allowing the creation of preferential hydraulic pathways.

- The Tromm granite is a suitable site for GeoLaB, as the composition is generally homogeneous and representative for the reservoirs of the URG, a high fracture density and connectivity was observed, the stress conditions and fracture orientation are favourable for reactivation, the hydraulic boundary conditions are controllable, and a sufficient overburden is ensured.

Data Availability Statement

550 The presented research data can be found at https://doi.org/10.48328/tudatalib-632 (Frey et al., 2021b).

Contributions of each author

Matthis Frey: Conceptualization, Data curation, Formal analysis, Investigation, Methodology, Validation, Visualization, Writing – original draft

Dr. Claire Bossennec: Conceptualization, Investigation, Methodology, Writing – review & editing

555 Lukas Seib: Investigation, Writing – review & editing

Dr. Kristian Bär: Funding acquisition, Project administration,Supervision, Writing – review & editing

Prof. Dr. Eva Schill: Resources, Conceptualization, Writing – review & editing

Prof. Dr. Ingo Sass: Resources, Supervision, Writing – review & editing

Competing Interest

560 We have no conflicts of interest to disclose.

References

Afshari, M., Valley, B., and Evans, K.: Scaling of Fracture Patterns in Three Deep Boreholes and Implications for Constraining Fractal Discrete Fracture Network Models, Rock Mech Rock Eng, 52, 1723–1743, https://doi.org/10.1007/s00603-019-1739-7, 2019.

575 Agemar, T., Alten, J.-A., Ganz, B., Kuder, J., Kühne, K., Schumacher, S., and Schulz, R.: The Geothermal Information System for Germany – GeotIS, Zeitschrift der Deutschen Gesellschaft für Geowissenschaften, 165, 129–144, https://doi.org/10.1127/1860-1804/2014/0060, 2014.

Altenberger, U. and Besch, T.: The Böllstein Odenwald: evidence for pre- to early Variscan plate convergence in the Central European variscides, International Journal of Earth Sciences, 82, 475–488,
580 https://doi.org/10.1007/BF00212411, 1993.

Altherr, R., Henes-Klaiber, U., Hegner, E., Satir, M., and Langer, C.: Plutonism in the Variscan Odenwald (Germany): from subduction to collision, International Journal of Earth Sciences, 88, 422–443, https://doi.org/10.1007/s005310050276, 1999.

Altwegg, P., Schill, E., Abdelfettah, Y., Radogna, P. V., and Mauri, G.: Toward fracture porosity assessment by
585 gravity forward modeling for geothermal exploration (Sankt Gallen, Switzerland), Geothermics, 57, 26–38, https://doi.org/10.1016/j.geothermics.2015.05.006, 2015.

Amstutz, G. C., Meisl, S., and Nickel, E. (Eds.): Mineralien und Gesteine im Odenwald, Heidelberg, 1975.

Bächler, D., Kohl, T., and Rybach, L.: Impact of graben-parallel faults on hydrothermal convection—Rhine Graben case study, Physics and Chemistry of the Earth, Parts A/B/C, 28, 431–441,
590 https://doi.org/10.1016/S1474-7065(03)00063-9, 2003.

Baillieux, P., Schill, E., Edel, J. B., and Mauri, G.: Localization of temperature anomalies in the Upper Rhine Graben: insights from geophysics and neotectonic activity, International Geology Review, 55, 1744–1762, https://doi.org/10.1080/00206814.2013.794914, 2013.

Bär, K., Reinecker, J., Bott, J., Cacace, M., Frey, M., van der Vaart, J., Scheck-Wenderoth, M., Ritter, O., Homuth,
595 B., Fritsche, J.-G., Spath, F., and Sass, I.: Integrated Exploration Strategy 'ConvEx' to detect Hydrothermal Convection in the Subsurface, in: Proceedings, Reykjavik, Iceland, April - October 2021, 2021.

Baskaran, M.: Radon: A Tracer for Geological, Geophysical and Geochemical Studies, Springer International Publishing, 260 pp., 2016.

Baujard, C., Genter, A., Dalmais, E., Maurer, V., Hehn, R., Rosillette, R., Vidal, J., and Schmittbuhl, J.:
600 Hydrothermal characterization of wells GRT-1 and GRT-2 in Rittershoffen, France: Implications on the understanding of natural flow systems in the rhine graben, Geothermics, 65, 255–268, https://doi.org/10.1016/j.geothermics.2016.11.001, 2017.

Bertrand, L., Géraud, Y., Le Garzic, E., Place, J., Diraison, M., Walter, B., and Haffen, S.: A multiscale analysis of a fracture pattern in granite: A case study of the Tamariu granite, Catalunya, Spain, Journal of Structural
605 Geology, 78, 52–66, https://doi.org/10.1016/j.jsg.2015.05.013, 2015.

Bertrand, L., Jusseaume, J., Géraud, Y., Diraison, M., Damy, P.-C., Navelot, V., and Haffen, S.: Structural heritage, reactivation and distribution of fault and fracture network in a rifting context: Case study of the western shoulder of the Upper Rhine Graben, Journal of Structural Geology, 108, 243–255, https://doi.org/10.1016/j.jsg.2017.09.006, 2018.

610 Biber, K., Khan, S. D., Seers, T. D., Sarmiento, S., and Lakshmikantha, M. R.: Quantitative characterization of a naturally fractured reservoir analog using a hybrid lidar-gigapixel imaging approach, Geosphere, 14, 710–730, https://doi.org/10.1130/GES01449.1, 2018.

Bisdom, K., Nick, H. M., and Bertotti, G.: An integrated workflow for stress and flow modelling using outcrop-derived discrete fracture networks, Computers & Geosciences, 103, 21–35, https://doi.org/10.1016/j.cageo.2017.02.019, 2017.

615

Bossennec, C., Frey, M., Seib, L., Bär, K., and Sass, I.: Multiscale Characterisation of Fracture Patterns of a Crystalline Reservoir Analogue, Geosciences, 11, https://doi.org/10.3390/geosciences11090371, 2021.

Bossennec, C., Seib, L., Frey, M., van der Vaart, J., and Sass, I.: Structural Architecture and Permeability Patterns of Crystalline Reservoir Rocks in the Northern Upper Rhine Graben: Insights from Surface Analogues of the

620

Odenwald, Energies, 15, 1310, https://doi.org/10.3390/en15041310, 2022.

Caine, J. S., Evans, J. P., and Forster, C. B.: Fault zone architecture and permeability structure, Geology, 24, 1025, https://doi.org/10.1130/0091-7613(1996)024<1025:FZAAPS>2.3.CO;2, 1996.

Chabani, A., Trullenque, G., L., B. A., and Klee, J.: Multiscale Characterization of Fracture Patterns: A Case Study of the Noble Hills Range (Death Valley, CA, USA), Application to Geothermal Reservoirs, Geosciences, 11,

625

280, https://doi.org/10.3390/geosciences11070280, 2021.

Cuenot, N., Faucher, J.-P., Fritsch, D., Genter, A., and Szablinski, D.: The European EGS project at Soultz-sous-Forêts: From extensive exploration to power production, in: Conversion and delivery of electrical energy in the 21st century: 2008 IEEE Power and Energy Society general meeting ; 20 - 24 July 2008, Pittsburgh, Pennsylvania, Pittsburgh, PA, 7/20/2008 - 7/24/2008, 1–8, 2008.

630

Deckert, H., Bauer, W., Abe, S., Horowitz, F., and Schneider, U.: Geophysical greenfield exploration in the permo-carboniferous Saar–Nahe basin—The Wiesbaden Geothermal Project, Germany, Geophysical Prospecting, 66, https://doi.org/10.1111/1365-2478.12598, 2017.

Dezayes, C., Lerouge, C., Innocent, C., and Lach, P.: Structural control on fluid circulation in a graben system: Constraints from the Saint Pierre Bois quarry (Vosges, France), Journal of Structural Geology, 146, 104323,

635

https://doi.org/10.1016/j.jsg.2021.104323, 2021.

Dezayes, C., Genter, A., and Valley, B.: Structure of the low permeable naturally fractured geothermal reservoir at Soultz, Comptes Rendus Geoscience, 342, 517–530, https://doi.org/10.1016/j.crte.2009.10.002, 2010.

Dezayes, C., Gentier, S., and Genter, A.: Deep Geothermal Energy in Western Europe: The Soultz-Project: Final Report, BRGM/RP-54227-FR, BRGM, 48 pp., 2005a.

640

Dezayes, C., Chevremont, P., Tourlière, B., Homeier, G., and Genter, A.: Geological study of the GPK4 HFR borehole and correlation with the GPK3 borehole (Soultz-sous-Forêts, France), BRGM, BRGM/RP-53697-FR, 2005b.

Drews, T., Miernik, G., Anders, K., Höfle, B., Profe, J., Emmerich, A., and Bechstädt, T.: Validation of fracture data recognition in rock masses by automated plane detection in 3D point clouds, International Journal of Rock

645

Mechanics and Mining Sciences, 109, 19–31, https://doi.org/10.1016/j.ijrmms.2018.06.023, 2018.

Duwiquet, H., Guillou-Frottier, L., Arbaret, L., Bellanger, M., Guillon, T., and Heap, M. J.: Crustal Fault Zones (CFZ) as Geothermal Power Systems: A Preliminary 3D THM Model Constrained by a Multidisciplinary Approach, Geofluids, 2021, 1–24, https://doi.org/10.1155/2021/8855632, 2021.

Egert, R., Korzani, M. G., Held, S., and Kohl, T.: Implications on large-scale flow of the fractured EGS reservoir

650

Soultz inferred from hydraulic data and tracer experiments, Geothermics, 84, 101749, https://doi.org/10.1016/j.geothermics.2019.101749, 2020.

Evans, K. F., Genter, A., and Sausse, J.: Permeability creation and damage due to massive fluid injections into granite at 3.5 km at Soultz: 1. Borehole observations, J. Geophys. Res., 110, https://doi.org/10.1029/2004JB003168, 2005.

655 Faulkner, D. R., Jackson, C., Lunn, R. J., Schlische, R. W., Shipton, Z. K., Wibberley, C., and Withjack, M. O.: A review of recent developments concerning the structure, mechanics and fluid flow properties of fault zones, Journal of Structural Geology, 32, 1557–1575, https://doi.org/10.1016/j.jsg.2010.06.009, 2010.

Fisher, J. E., Shakoor, A., and Watts, C. F.: Comparing discontinuity orientation data collected by terrestrial LiDAR and transit compass methods, Engineering Geology, 181, 78–92,
660 https://doi.org/10.1016/j.enggeo.2014.08.014, 2014.

Frey, M., Weinert, S., Bär, K., van der Vaart, J., Dezayes, C., Calcagno, P., and Sass, I.: Integrated 3D geological modelling of the northern Upper Rhine Graben by joint inversion of gravimetry and magnetic data, Tectonophysics, 813, 228927, https://doi.org/10.1016/j.tecto.2021.228927, 2021a.

Frey, M., Bossennec, C., Seib, L., Bär, K., and Sass, I.: Interdisciplinary Dataset on the Fracture Network of the
665 Tromm Granite, Southern Odenwald, SW Germany, 2021b.

Freymark, J., Sippel, J., Scheck-Wenderoth, M., Bär, K., Stiller, M., Fritsche, J.-G., and Kracht, M.: The deep thermal field of the Upper Rhine Graben, Tectonophysics, 694, 114–129, https://doi.org/10.1016/j.tecto.2016.11.013, available at: http://www.sciencedirect.com/science/article/pii/S0040195116305297, 2017.

670 Genter, A. and Traineau, H.: Analysis of macroscopic fractures in granite in the HDR geothermal well EPS-1, Soultz-sous-Foreˆts, France, Journal of Volcanology and Geothermal Research, 72, 121–141, https://doi.org/10.1016/0377-0273(95)00070-4, 1996.

Genter, A., Castaing, C., Dezayes, C., Tenzer, H., Traineau, H., and Villemin, T.: Comparative analysis of direct (core) and indirect (borehole imaging tools) collection of fracture data in the Hot Dry Rock Soultz reservoir
675 (France), J. Geophys. Res., 102, 15419–15431, https://doi.org/10.1029/97JB00626, 1997.

Genter, A., Evans, K., Cuenot, N., Fritsch, D., and Sanjuan, B.: Contribution of the exploration of deep crystalline fractured reservoir of Soultz to the knowledge of enhanced geothermal systems (EGS), Comptes Rendus Geoscience, 342, 502–516, https://doi.org/10.1016/j.crte.2010.01.006, 2010.

Glaas, C., Vidal, J., and Genter, A.: Structural characterization of naturally fractured geothermal reservoirs in the
680 central Upper Rhine Graben, Journal of Structural Geology, 148, 104370, https://doi.org/10.1016/j.jsg.2021.104370, 2021.

Guerriero, V., Vitale, S., Ciarcia, S., and Mazzoli, S.: Improved statistical multi-scale analysis of fractured reservoir analogues, Tectonophysics, 504, 14–24, https://doi.org/10.1016/j.tecto.2011.01.003, 2011.

Guglielmetti, L., Comina, C., Abdelfettah, Y., Schill, E., and Mandrone, G.: Integration of 3D geological modeling
685 and gravity surveys for geothermal prospection in an Alpine region, Tectonophysics, 608, 1025–1036, https://doi.org/10.1016/j.tecto.2013.07.012, 2013.

Guillen, A., Calcagno, P., Courrioux, G., Joly, A., and Ledru, P.: Geological modelling from field data and geological knowledge, Part II, Modelling validation using gravity and magnetic data inversion, Physics of the Earth and Planetary Interiors, 171, 158–169, https://doi.org/10.1016/j.pepi.2008.06.014, 2008.

690 Guillou-Frottier, L., Carrè, C., Bourgine, B., Bouchot, V., and Genter, A.: Structure of hydrothermal convection in the Upper Rhine Graben as inferred from corrected temperature data and basin-scale numerical models,

30

Journal of Volcanology and Geothermal Research, 256, 29–49,
https://doi.org/10.1016/j.jvolgeores.2013.02.008, 2013.

Hess, J. C. and Schmidt, G.: Zur Altersstellung der Kataklasite im Bereich der Otzberg-Zone, Odenwald, Geol Jb
695 Hessen, 117, 69–77, 1989.

HLUG: Geologische Karte von Hessen, Hessisches Landesamt für Umwelt und Geologie, 2007.

Ioannides, K., Papachristodoulou, C., Stamoulis, K., Karamanis, D., Pavlides, S., Chatzipetros, A., and Karakala, E.:
Soil gas radon: a tool for exploring active fault zones, Applied Radiation and Isotopes, 59, 205–213,
https://doi.org/10.1016/S0969-8043(03)00164-7, 2003.

700 Jing, L. and Stephansson, O.: Fundamentals of discrete element methods for rock engineering: theory and
applications, Elsevier, 2007.

Jolie, E., Klinkmueller, M., Moeck, I., and Bruhn, D.: Linking gas fluxes at Earth's surface with fracture zones in an
active geothermal field, Geology, 44, 187–190, https://doi.org/10.1130/G37412.1, 2016.

Jolie, E., Klinkmueller, M., and Moeck, I.: Diffuse surface emanations as indicator of structural permeability in
705 fault-controlled geothermal systems, Journal of Volcanology and Geothermal Research, 290, 97–113,
https://doi.org/10.1016/j.jvolgeores.2014.11.003, 2015.

King, C.-Y., King, B.-S., Evans, W. C., and Zhang, W.: Spatial radon anomalies on active faults in California,
Applied Geochemistry, 11, 497–510, https://doi.org/10.1016/0883-2927(96)00003-0, 1996.

Klemm, G.: Geologische Karte von Hessen - Blatt 6318 Lindenfels, Hessischer Staatsverlag, Darmstadt, 1933.

710 Klemm, G.: Geologische Karte von Hessen - Blatt 6418 Birkenau (Weinheim), Hessischer Staatsverlag,
Darmstadt, 1929.

Klemm, G.: Geologische Karte von Hessen - Blatt 6319 Erbach, Hessischer Staatsverlag, Darmstadt, 1928.

Klemm, G.: Geologische Karte des Großherzogtums Hessen - Blatt 6419 Beerfelden, Darmstadt, 1900.

Kreuzer, H. and Harre, W.: K/Ar-Altersbestimmungen an Hornblenden und Biotiten des Kristallinen Odenwalds,
715 in: Mineralien und Gesteine im Odenwald, edited by: Amstutz, G. C., Meisl, S., and Nickel, E., Heidelberg,
70–78, 1975.

Krohe, A.: Structural evolution of intermediate-crustal rocks in a strike-slip and extensional setting (Variscan
Odenwald, SW Germany): differential upward transport of metamorphic complexes and changing
deformation mechanisms, Tectonophysics, 205, 357–386, https://doi.org/10.1016/0040-1951(92)90443-A,
720 1992.

Krohe, A.: Emplacement of synkinematic plutons in the Variscan Odenwald (Germany) controlled by
transtensional tectonics, International Journal of Earth Sciences, 80, 391–409,
https://doi.org/10.1007/BF01829373, 1991.

Krohe, A. and Willner, A. P.: IV.C.2 The Odenwald Crystalline Complex, in: Pre-Permian Geology of Central and
725 Eastern Europe, edited by: Dallmeyer, R. D., Franke, W., and Weber, K., Springer Berlin Heidelberg, Berlin,
Heidelberg, 182–185, 1995.

Ledésert, B., Hebert, R., Genter, A., Bartier, D., Clauer, N., and Grall, C.: Fractures, hydrothermal alterations and
permeability in the Soultz Enhanced Geothermal System, Comptes Rendus Geoscience, 342, 607–615,
https://doi.org/10.1016/j.crte.2009.09.011, 2010.

730 Li, Y. and Oldenburg, D. W.: 3-D inversion of gravity data, GEOPHYSICS, 63, 109–119, 1998.

Maggetti, M.: Die Tiefengesteine des Bergsträßer Odenwaldes, in: Mineralien und Gesteine im Odenwald, edited by: Amstutz, G. C., Meisl, S., and Nickel, E., Heidelberg, 87–109, 1975.

Mahmoodpour, S., Singh, M., Turan, A., Bär, K., and Sass, I.: Hydro-Thermal Modeling for Geothermal Energy Extraction from Soultz-sous-Forêts, France, Geosciences, 11, 464, https://doi.org/10.3390/geosciences11110464, 2021.

Mahmoodpour, S., Singh, M., Turan, A., Bär, K., and Sass, I.: Key parameters affecting the performance of fractured geothermal reservoirs: a sensitivity analysis by thermo-hydraulic-mechanical simulation, Energy, in review.

Marrett, R., Ortega, O. J., and Kelsey, C. M.: Extent of power-law scaling for natural fractures in rock, Geology, 27, 799, https://doi.org/10.1130/0091-7613(1999)027%3C0799:EOPLSF%3E2.3.CO;2, 1999.

McCaffrey, K., Lonergan, L., and Wilkinson, J. (Eds.): Fractures, fluid flow and mineralization, 1999.

McCubbine, J., Tontini, F. C., Stagpoole, V., Smith, E., and O'Brien, G.: Gsolve, a Python computer program with a graphical user interface to transform relative gravity survey measurements to absolute gravity values and gravity anomalies, SoftwareX, 7, 129–137, https://doi.org/10.1016/j.softx.2018.04.003, 2018.

Meixner, J., Grimmer, J. C., Becker, A., Schill, E., and Kohl, T.: Comparison of different digital elevation models and satellite imagery for lineament analysis: Implications for identification and spatial arrangement of fault zones in crystalline basement rocks of the southern Black Forest (Germany), Journal of Structural Geology, 108, 256–268, https://doi.org/10.1016/j.jsg.2017.11.006, 2018.

Meller, C. and Ledésert, B.: Is There a Link Between Mineralogy, Petrophysics, and the Hydraulic and Seismic Behaviors of the Soultz-sous-Forêts Granite During Stimulation? A Review and Reinterpretation of Petro-Hydromechanical Data Toward a Better Understanding of Induced Seismicity, J. Geophys. Res., 122, 9755–9774, https://doi.org/10.1002/2017JB014648, 2017.

Nettleton, L. L.: DETERMINATION OF DENSITY FOR REDUCTION OF GRAVIMETER OBSERVATIONS*, GEOPHYSICS, 4, 176–183, https://doi.org/10.1190/1.0403176, 1939.

Nickel, E.: Geologische Position und Petrogenese des kristallinen Odenwaldes, in: Mineralien und Gesteine im Odenwald, edited by: Amstutz, G. C., Meisl, S., and Nickel, E., Heidelberg, 1–25, 1975.

Niven, E. B. and Deutsch, C. V.: A sensitivity analysis for equivalent permeability tensors calculated from 2D discrete fracture networks, CCG Ann. Rep, 11, 1–8, 2009.

Oda, M.: Permeability tensor for discontinuous rock masses, Géotechnique, 35, 483–495, https://doi.org/10.1680/geot.1985.35.4.483, 1985.

Okrusch, M., Schubert, W., and Nasir, S.: IV.D Igneous Activity (Pre- to Early Variscan Magmatism), in: Pre-Permian Geology of Central and Eastern Europe, edited by: Dallmeyer, R. D., Franke, W., and Weber, K., Springer Berlin Heidelberg, Berlin, Heidelberg, 190–200, 1995.

Okrusch, M., Raumer, J. von, Matthes, S., and Schubert, W.: Mineralfazies und Stellung der Metamorphite im kristallinen Odenwald, in: Mineralien und Gesteine im Odenwald, edited by: Amstutz, G. C., Meisl, S., and Nickel, E., Heidelberg, 109–134, 1975.

Pickering, G., Bull, J. M., and Sanderson, D. J.: Sampling power-law distributions, Tectonophysics, 248, 1–20, https://doi.org/10.1016/0040-1951(95)00030-Q, 1995.

Place, J., Géraud, Y., Diraison, M., Herquel, G., Edel, J. B., Bano, M., Le Garzic, E., and Walter, B.: Structural control of weathering processes within exhumed granitoids: Compartmentalisation of geophysical

properties by faults and fractures, Journal of Structural Geology, 84, 102–119, https://doi.org/10.1016/j.jsg.2015.11.011, 2016.

Poller, U., Altenberger, U., and Schubert, W.: Geochemical investigations of the Bergsträsser Odenwald amphibolites - implicationsfor back-arc magmatism, Mineralogy and Petrology, 72, 63–76,

775   https://doi.org/10.1007/s007100170027, 2001.

Pribnow, D. and Schellschmidt, R.: Thermal tracking of upper crustal fluid flow in the Rhine graben, Geophys. Res. Lett., 27, 1957–1960, https://doi.org/10.1029/2000GL008494, 2000.

Rathnaweera, T. D., Wu, W., Ji, Y., and Gamage, R. P.: Understanding injection-induced seismicity in enhanced geothermal systems: From the coupled thermo-hydro-mechanical-chemical process to anthropogenic

780   earthquake prediction, Earth-Science Reviews, 205, 103182, https://doi.org/10.1016/j.earscirev.2020.103182, 2020.

Reischmann, T., Anthes, G., Jaeckel, P., and Altenberger, U.: Age and origin of the Böllsteiner Odenwald, Mineralogy and Petrology, 72, 29–44, https://doi.org/10.1007/s007100170025, 2001.

Reiter, K., Heidbach, O., Müller, B., Reinecker, J., Röckl, T., Reiter, K., Heidbach, O., Müller, B., Reinecker, J., and

785   Röckel, T.: Stress Map Germany 2016, https://doi.org/10.5880/WSM.Germany2016_en, 2016.

Sanderson, D. J. and Nixon, C. W.: Topology, connectivity and percolation in fracture networks, Journal of Structural Geology, 115, 167–177, https://doi.org/10.1016/j.jsg.2018.07.011, 2018.

Sausse, J. and Genter, A.: Types of permeable fractures in granite, Geological Society, London, Special Publications, 240, 1–14, https://doi.org/10.1144/GSL.SP.2005.240.01.01, 2005.

790 Sausse, J., Dezayes, C., Dorbath, L., Genter, A., and Place, J.: 3D model of fracture zones at Soultz-sous-Forêts based on geological data, image logs, induced microseismicity and vertical seismic profiles, Comptes Rendus Geoscience, 342, 531–545, https://doi.org/10.1016/j.crte.2010.01.011, 2010.

Schälicke, W.: Die Otzberg-Zone, in: Mineralien und Gesteine im Odenwald, edited by: Amstutz, G. C., Meisl, S., and Nickel, E., Heidelberg, 47–59, 1975.

795 Schill, E., Genter, A., Cuenot, N., and Kohl, T.: Hydraulic performance history at the Soultz EGS reservoirs from stimulation and long-term circulation tests, Geothermics, 70, 110–124, https://doi.org/10.1016/j.geothermics.2017.06.003, 2017.

Schill, E., Meixner, J., Meller, C., Grimm, M., Grimmer, J. C., Stober, I., and Kohl, T.: Criteria and geological setting for the generic geothermal underground research laboratory, GEOLAB, Geotherm Energy, 4,

800   https://doi.org/10.1186/s40517-016-0049-5, 2016.

Schubert, W., Lippolt, H. J., and Schwarz, W.: Early to Middle Carboniferous hornblende 40 Ar/ 39 Ar ages of amphibolites and gabbros from the Bergsträsser Odenwald, Mineralogy and Petrology, 72, 113–132, https://doi.org/10.1007/s007100170029, 2001.

Snow, D. T.: A parallel plate model of fractured permeable media, University of California, Berkeley, 1965.

805 Stein, E.: The geology of the Odenwald Crystalline Complex, Mineralogy and Petrology, 72, 7–28, https://doi.org/10.1007/s007100170024, 2001.

Stober, I. and Bucher, K.: Hydraulic properties of the crystalline basement, Hydrogeol J, 15, 213–224, https://doi.org/10.1007/s10040-006-0094-4, 2007.

Todt, W. A., Altenberger, U., and Raumer, J. F. von: U-Pb data on zircons for the thermal peak of metamorphism in the Variscan Odenwald, Germany, Geologische Rundschau, 84, 466–472, https://doi.org/10.1007/BF00284514, 1995.

Traineau, H., Genter, A., Cautru, J. P., Fabriol, H., and Chèvremont, P.: Petrography of the granite massif from drill cutting analysis and well log interpretation in the geothermal HDR borehole GPK1 (Soultz, Alsace, France), Geothermal science and technology, 3, 1–29, 1991.

Tranter, M., Lucia, M. de, and Kühn, M.: Numerical investigation of barite scaling kinetics in fractures, Geothermics, 91, 102027, https://doi.org/10.1016/j.geothermics.2020.102027, 2021.

van Zyl, J. J.: The Shuttle Radar Topography Mission (SRTM): a breakthrough in remote sensing of topography, Acta Astronautica, 48, 559–565, https://doi.org/10.1016/S0094-5765(01)00020-0, 2001.

Vazaios, I., Vlachopoulos, N., and Diederichs, M. S.: Integration of Lidar-Based Structural Input and Discrete Fracture Network Generation for Underground Applications, Geotech Geol Eng, 35, 2227–2251, https://doi.org/10.1007/s10706-017-0240-x, 2017.

Vidal, J. and Genter, A.: Overview of naturally permeable fractured reservoirs in the central and southern Upper Rhine Graben: Insights from geothermal wells, Geothermics, 74, 57–73, https://doi.org/10.1016/j.geothermics.2018.02.003, 2018.

Vidal, J., Genter, A., and Chopin, F.: Permeable fracture zones in the hard rocks of the geothermal reservoir at Rittershoffen, France, J. Geophys. Res., 122, 4864–4887, https://doi.org/10.1002/2017JB014331, 2017.

Vidal, J., Patrier, P., Genter, A., Beaufort, D., Dezayes, C., Glaas, C., Lerouge, C., and Sanjuan, B.: Clay minerals related to the circulation of geothermal fluids in boreholes at Rittershoffen (Alsace, France), Journal of Volcanology and Geothermal Research, 349, 192–204, https://doi.org/10.1016/j.jvolgeores.2017.10.019, 2018.

Vogt, C., Marquart, G., Kosack, C., Wolf, A., and Clauser, C.: Estimating the permeability distribution and its uncertainty at the EGS demonstration reservoir Soultz-sous-Forêts using the ensemble Kalman filter, Water Resour. Res., 48, https://doi.org/10.1029/2011WR011673, 2012.

Weinert, S., Bär, K., and Sass, I.: Petrophysical Properties of the Mid-German Crystalline High: A Database for Bavarian, Hessian, Rhineland-Palatinate and Thuringian Outcrops, 2020.

Welsch, B., Rühaak, W., Schulte, D. O., Bär, K., and Sass, I.: Characteristics of medium deep borehole thermal energy storage, Int. J. Energy Res., 40, 1855–1868, https://doi.org/10.1002/er.3570, 2016.

Zeng, Q., Lu, W., Zhang, R., Zhao, J., Ren, P., and Wang, B.: LIDAR-based fracture characterization and controlling factors analysis: An outcrop case from Kuqa Depression, NW China, Journal of Petroleum Science and Engineering, 161, 445–457, https://doi.org/10.1016/j.petrol.2017.12.002, 2018.

Zhang, Y., Person, M., Rupp, J., Ellett, K., Celia, M. A., Gable, C. W., Bowen, B., Evans, J., Bandilla, K., Mozley, P., Dewers, T., and Elliot, T.: Hydrogeologic controls on induced seismicity in crystalline basement rocks due to fluid injection into basal reservoirs, Ground water, 51, 525–538, https://doi.org/10.1111/gwat.12071, 2013.